Nonprompt direct-photon production in Au+Au collisions at √ =200 GeV

(PHENIX Collaboration) Abdulameer, N. J.; ...; Makek, M.; ...; Zou, L.

Nonprompt direct-photon production in Au+Au collisions at $\sqrt{s_{NN}} = 200$ GeV

N. J. Abdulameer,[16] U. Acharya,[21] A. Adare,[12] C. Aidala,[43] N. N. Ajitanand,[62,*] Y. Akiba,[57,58,†] M. Alfred,[23] N. Apadula,[28,63] H. Asano,[35,57] B. Azmoun,[7] V. Babintsev,[24] M. Bai,[6] N. S. Bandara,[41] B. Bannier,[63] K. N. Barish,[8] S. Bathe,[5,58] A. Bazilevsky,[7] M. Beaumier,[8] S. Beckman,[12] R. Belmont,[12,43,50] A. Berdnikov,[60] Y. Berdnikov,[60] L. Bichon,[68] B. Blankenship,[68] D. S. Blau,[34,47] J. S. Bok,[49] V. Borisov,[60] K. Boyle,[58] M. L. Brooks,[37] J. Bryslawskyj,[5,8] V. Bumazhnov,[24] S. Campbell,[13,14,28] V. Canoa Roman,[63] C.-H. Chen,[58] M. Chiu,[7] C. Y. Chi,[13,14] I. J. Choi,[25] J. B. Choi,[30,*] T. Chujo,[67] Z. Citron,[69] M. Connors,[21] R. Corliss,[63] Y. Corrales Morales,[37] M. Csanád,[17] T. Csörgő,[42,70] T. W. Danley,[51] A. Datta,[48] M. S. Daugherity,[1] G. David,[7,63] C. T. Dean,[37] K. DeBlasio,[48] K. Dehmelt,[63] A. Denisov,[24] A. Deshpande,[58,63] E. J. Desmond,[7] A. Dion,[63] P. B. Diss,[40] J. H. Do,[71] V. Doomra,[63] A. Drees,[63] K. A. Drees,[6] J. M. Durham,[37] A. Durum,[24] A. Enokizono,[57,59] R. Esha,[63] B. Fadem,[45] W. Fan,[63] N. Feege,[63] D. E. Fields,[48] M. Finger, Jr.,[48] M. Finger,[9] D. Firak,[16,63] D. Fitzgerald,[43] S. L. Fokin,[34] J. E. Frantz,[51] A. Franz,[7] A. D. Frawley,[20] P. Gallus,[15] C. Gal,[63] P. Garg,[3,63] H. Ge,[63] M. Giles,[63] F. Giordano,[25] A. Glenn,[36] Y. Goto,[57,58] N. Grau,[2] S. V. Greene,[68] M. Grosse Perdekamp,[25] T. Gunji,[11] T. Guo,[63] T. Hachiya,[46,57,58] J. S. Haggerty,[7] K. I. Hahn,[18] H. Hamagaki,[11] H. F. Hamilton,[1] J. Hanks,[63] S. Y. Han,[18,33] M. Harvey,[65] S. Hasegawa,[29] T. O. S. Haseler,[21] K. Hashimoto,[57,59] T. K. Hemmick,[63] X. He,[21] J. C. Hill,[28] A. Hodges,[21] R. S. Hollis,[8] K. Homma,[22] B. Hong,[33] T. Hoshino,[22] N. Hotvedt,[28] J. Huang,[7] K. Imai,[29] M. Inaba,[67] A. Iordanova,[8] D. Isenhower,[1] D. Ivanishchev,[55] B. V. Jacak,[63] M. Jezghani,[21] X. Jiang,[37] Z. Ji,[63] B. M. Johnson,[7,21] D. Jouan,[53] D. S. Jumper,[25] S. Kanda,[11] J. H. Kang,[71] D. Kawall,[41] A. V. Kazantsev,[34] J. A. Key,[48] V. Khachatryan,[63] A. Khanzadeev,[55] A. Khatiwada,[37] B. Kimelman,[45] C. Kim,[33] D. J. Kim,[31] E.-J. Kim,[30] G. W. Kim,[18] M. Kim,[61] T. Kim,[18] D. Kincses,[17] A. Kingan,[63] E. Kistenev,[7] R. Kitamura,[11] J. Klatsky,[20] D. Kleinjan,[8] P. Kline,[63] T. Koblesky,[12] B. Komkov,[55] D. Kotov,[55,60] L. Kovacs,[17] B. Kurgyis,[17] K. Kurita,[59] M. Kurosawa,[57,58] Y. Kwon,[71] J. G. Lajoie,[28] D. Larionova,[60] A. Lebedev,[28] S. Lee,[71] S. H. Lee,[28,43,63] M. J. Leitch,[37] N. A. Lewis,[43] S. H. Lim,[56,71] M. X. Liu,[37] X. Li,[10] X. Li,[37] D. A. Loomis,[43] D. Lynch,[7] S. Lökös,[17] T. Majoros,[16] Y. I. Makdisi,[6] M. Makek,[72] A. Manion,[63] V. I. Manko,[34] E. Mannel,[7] M. McCumber,[37] P. L. McGaughey,[37] D. McGlinchey,[12,37] C. McKinney,[25] A. Meles,[49] M. Mendoza,[8] A. C. Mignerey,[40] A. Milov,[69] D. K. Mishra,[4] J. T. Mitchell,[7] M. Mitrankova,[60] Iu. Mitrankov,[60] S. Miyasaka,[57,66] S. Mizuno,[57,67] A. Mohamed,[16] A. K. Mohanty,[4] M. M. Mondal,[63] P. Montuenga,[25] T. Moon,[33,71] D. P. Morrison,[7] T. V. Moukhanova,[34] B. Mulilo,[33,57,73] T. Murakami,[35,57] J. Murata,[57,59] A. Mwai,[62] K. Nagashima,[22] J. L. Nagle,[12] M. I. Nagy,[17] I. Nakagawa,[57,58] H. Nakagomi,[57,67] K. Nakano,[57,66] C. Nattrass,[64] S. Nelson,[19] P. K. Netrakanti,[4] T. Niida,[67] S. Nishimura,[11] R. Nouicer,[7,58] N. Novitzky,[31,63,67] T. Novák,[42,70] G. Nukazuka,[57,58] A. S. Nyanin,[34] E. O'Brien,[7] C. A. Ogilvie,[28] J. D. Orjuela Koop,[12] M. Orosz,[16] J. D. Osborn,[43,52] A. Oskarsson,[38] K. Ozawa,[32,67] R. Pak,[7] V. Pantuev,[26] V. Papavassiliou,[49] J. S. Park,[61] S. Park,[44,61,63] M. Patel,[28] S. F. Pate,[49] J.-C. Peng,[25] W. Peng,[68] D. V. Perepelitsa,[7,12] G. D. N. Perera,[49] D. Yu. Peressounko,[34] C. E. PerezLara,[63] J. Perry,[28] R. Petti,[7,63] C. Pinkenburg,[7] R. Pinson,[1] R. P. Pisani,[7] M. Potekhin,[7] A. Pun,[51] M. L. Purschke,[7] P. V. Radzevich,[60] J. Rak,[31] N. Ramasubramanian,[63] B. J. Ramson,[43] I. Ravinovich,[69] K. F. Read,[52,64] D. Reynolds,[62] V. Riabov,[47,55] Y. Riabov,[55,60] D. Richford,[5] T. Rinn,[25,28] S. D. Rolnick,[8] M. Rosati,[28] Z. Rowan,[5] J. G. Rubin,[43] J. Runchey,[28] B. Sahlmueller,[63] N. Saito,[32] T. Sakaguchi,[7] H. Sako,[29] V. Samsonov,[47,55] M. Sarsour,[21] S. Sato,[29] B. Schaefer,[68] B. K. Schmoll,[64] K. Sedgwick,[8] R. Seidl,[57,58] A. Sen,[28,64] R. Seto,[8] P. Sett,[4] A. Sexton,[40] D. Sharma,[63] I. Shein,[24] Z. Shi,[37] M. Shibata,[46] T.-A. Shibata,[57,66] K. Shigaki,[22] M. Shimomura,[28,46] P. Shukla,[4] A. Sickles,[7,25] C. L. Silva,[37] D. Silvermyr,[38,52] B. K. Singh,[3] C. P. Singh,[3] V. Singh,[3] M. Slunečka,[9] K. L. Smith,[20] M. Snowball,[37] R. A. Soltz,[36] W. E. Sondheim,[37] S. P. Sorensen,[64] I. V. Sourikova,[7] P. W. Stankus,[52] M. Stepanov,[41,*] S. P. Stoll,[7] T. Sugitate,[22] A. Sukhanov,[7] T. Sumita,[57] J. Sun,[63] Z. Sun,[16] J. Sziklai,[70] R. Takahama,[46] A. Taketani,[57,58] K. Tanida,[29,58,61] M. J. Tannenbaum,[7] S. Tarafdar,[68,69] A. Taranenko,[47,62] R. Tieulent,[21,39] A. Timilsina,[28] T. Todoroki,[57,58,67] M. Tomášek,[15] C. L. Towell,[1] R. Towell,[1] R. S. Towell,[1] I. Tserruya,[69] Y. Ueda,[22] B. Ujvari,[16] H. W. van Hecke,[37] J. Velkovska,[68] M. Virius,[15] V. Vrba,[15,27] X. R. Wang,[49,58] Z. Wang,[5] Y. Watanabe,[57,58] Y. S. Watanabe,[11,32] F. Wei,[49] A. S. White,[43] C. P. Wong,[21,37] C. L. Woody,[7] M. Wysocki,[52] B. Xia,[51] L. Xue,[21] S. Yalcin,[63] Y. L. Yamaguchi,[11,63] A. Yanovich,[24] Z. Yin,[63] I. Yoon,[61] J. H. Yoo,[33] I. E. Yushmanov,[34] H. Yu,[49,54] W. A. Zajc,[13,14] A. Zelenski,[6] S. Zhou,[10] and L. Zou[8]

(PHENIX Collaboration)

[1]*Abilene Christian University, Abilene, Texas 79699, USA*

[2]*Department of Physics, Augustana University, Sioux Falls, South Dakota 57197, USA*

[3]*Department of Physics, Banaras Hindu University, Varanasi 221005, India*

[4]*Bhabha Atomic Research Centre, Bombay 400 085, India*

[5]*Baruch College, City University of New York, New York, New York 10010, USA*

[6]*Collider-Accelerator Department, Brookhaven National Laboratory, Upton, New York 11973-5000, USA*

[*]Deceased.

[†]PHENIX spokesperson: akiba@rcf.rhic.bnl.gov

[7]*Physics Department, Brookhaven National Laboratory, Upton, New York 11973-5000, USA*
[8]*University of California–Riverside, Riverside, California 92521, USA*
[9]*Faculty of Mathematics and Physics, Charles University, 180 00 Troja, Prague, Czech Republic*
[10]*Science and Technology on Nuclear Data Laboratory, China Institute of Atomic Energy, Beijing 102413, People's Republic of China*
[11]*Center for Nuclear Study, Graduate School of Science, University of Tokyo, 7-3-1 Hongo, Bunkyo, Tokyo 113-0033, Japan*
[12]*University of Colorado, Boulder, Colorado 80309, USA*
[13]*Columbia University, New York, New York 10027, USA*
[14]*Nevis Laboratories, Irvington, New York 10533, USA*
[15]*Czech Technical University, Zikova 4, 166 36 Prague 6, Czech Republic*
[16]*Debrecen University, Egyetem tér 1, H-4010 Debrecen, Hungary*
[17]*ELTE, Eötvös Loránd University, Pázmány P.s. 1/A, H-1117 Budapest, Hungary*
[18]*Ewha Womans University, Seoul 120-750, Korea*
[19]*Florida A&M University, Tallahassee, Florida 32307, USA*
[20]*Florida State University, Tallahassee, Florida 32306, USA*
[21]*Georgia State University, Atlanta, Georgia 30303, USA*
[22]*Hiroshima University, Kagamiyama, Higashi-Hiroshima 739-8526, Japan*
[23]*Department of Physics and Astronomy, Howard University, Washington, DC 20059, USA*
[24]*IHEP Protvino, State Research Center of Russian Federation, Institute for High Energy Physics, Protvino 142281, Russia*
[25]*University of Illinois at Urbana-Champaign, Urbana, Illinois 61801, USA*
[26]*Institute for Nuclear Research of the Russian Academy of Sciences, Prospekt 60 Letiya Oktyabrya 7a, Moscow 117312, Russia*
[27]*Institute of Physics, Academy of Sciences of the Czech Republic, Na Slovance 2, 182 21 Prague 8, Czech Republic*
[28]*Iowa State University, Ames, Iowa 50011, USA*
[29]*Advanced Science Research Center, Japan Atomic Energy Agency, 2-4 Shirakata Shirane, Tokai-mura, Naka-gun, Ibaraki-ken 319-1195, Japan*
[30]*Jeonbuk National University, Jeonju 54896, Korea*
[31]*Helsinki Institute of Physics and University of Jyväskylä, P.O. Box 35, FI-40014 Jyväskylä, Finland*
[32]*KEK, High Energy Accelerator Research Organization, Tsukuba, Ibaraki 305-0801, Japan*
[33]*Korea University, Seoul 02841, Korea*
[34]*National Research Center "Kurchatov Institute", Moscow 123098, Russia*
[35]*Kyoto University, Kyoto 606-8502, Japan*
[36]*Lawrence Livermore National Laboratory, Livermore, California 94550, USA*
[37]*Los Alamos National Laboratory, Los Alamos, New Mexico 87545, USA*
[38]*Department of Physics, Lund University, Box 118, SE-221 00 Lund, Sweden*
[39]*IPNL, CNRS/IN2P3, Université Lyon, Université Lyon 1, F-69622 Villeurbanne, France*
[40]*University of Maryland, College Park, Maryland 20742, USA*
[41]*Department of Physics, University of Massachusetts, Amherst, Massachusetts 01003-9337, USA*
[42]*MATE, Laboratory of Femtoscopy, Károly Róbert Campus, Gyöngyös, Hungary*
[43]*Department of Physics, University of Michigan, Ann Arbor, Michigan 48109-1040, USA*
[44]*Mississippi State University, Mississippi State, Mississippi 39762, USA*
[45]*Muhlenberg College, Allentown, Pennsylvania 18104-5586, USA*
[46]*Nara Women's University, Kita-uoya Nishi-machi, Nara 630-8506, Japan*
[47]*National Research Nuclear University, MEPhI, Moscow Engineering Physics Institute, Moscow 115409, Russia*
[48]*University of New Mexico, Albuquerque, New Mexico 87131, USA*
[49]*New Mexico State University, Las Cruces, New Mexico 88003, USA*
[50]*Physics and Astronomy Department, University of North Carolina at Greensboro, Greensboro, North Carolina 27412, USA*
[51]*Department of Physics and Astronomy, Ohio University, Athens, Ohio 45701, USA*
[52]*Oak Ridge National Laboratory, Oak Ridge, Tennessee 37831, USA*
[53]*IPN-Orsay, Université Paris-Sud, CNRS/IN2P3, Université Paris-Saclay, BP 1, F-91406 Orsay, France*
[54]*Peking University, Beijing 100871, People's Republic of China*
[55]*PNPI, Petersburg Nuclear Physics Institute, Gatchina, Leningrad Region 188300, Russia*
[56]*Pusan National University, Pusan 46241, Korea*
[57]*RIKEN Nishina Center for Accelerator-Based Science, Wako, Saitama 351-0198, Japan*
[58]*RIKEN BNL Research Center, Brookhaven National Laboratory, Upton, New York 11973-5000, USA*
[59]*Physics Department, Rikkyo University, 3-34-1 Nishi-Ikebukuro, Toshima, Tokyo 171-8501, Japan*
[60]*Saint Petersburg State Polytechnic University, St. Petersburg 195251, Russia*
[61]*Department of Physics and Astronomy, Seoul National University, Seoul 151-742, Korea*
[62]*Chemistry Department, Stony Brook University, SUNY, Stony Brook, New York 11794-3400, USA*
[63]*Department of Physics and Astronomy, Stony Brook University, SUNY, Stony Brook, New York 11794-3800, USA*
[64]*University of Tennessee, Knoxville, Tennessee 37996, USA*

[65]*Texas Southern University, Houston, Texas 77004, USA*
[66]*Department of Physics, Tokyo Institute of Technology, Oh-okayama, Meguro, Tokyo 152-8551, Japan*
[67]*Tomonaga Center for the History of the Universe, University of Tsukuba, Tsukuba, Ibaraki 305, Japan*
[68]*Vanderbilt University, Nashville, Tennessee 37235, USA*
[69]*Weizmann Institute, Rehovot 76100, Israel*
[70]*Institute for Particle and Nuclear Physics, Wigner Research Centre for Physics, Hungarian Academy of Sciences (Wigner RCP, RMKI), P.O. Box 49, H-1525 Budapest 114, Hungary*
[71]*Yonsei University, IPAP, Seoul 120-749, Korea*
[72]*Department of Physics, Faculty of Science, University of Zagreb, Bijenička c. 32, HR-10002 Zagreb, Croatia*
[73]*Department of Physics, School of Natural Sciences, University of Zambia, Great East Road Campus, Box 32379, Lusaka, Zambia*

(Received 5 April 2022; revised 18 December 2023; accepted 26 January 2024; published 18 April 2024)

The measurement of the direct-photon spectrum from Au+Au collisions at $\sqrt{s_{NN}} = 200$ GeV is presented by the PHENIX Collaboration using the external-photon-conversion technique for 0%–93% central collisions in a transverse-momentum (p_T) range of 0.8–10 GeV/c. An excess of direct photons, above prompt-photon production from hard-scattering processes, is observed for $p_T < 6$ GeV/c. Nonprompt direct photons are measured by subtracting the prompt component, which is estimated as $N_{\rm coll}$-scaled direct photons from $p+p$ collisions at 200 GeV, from the direct-photon spectrum. Results are obtained for $0.8 < p_T < 6.0$ GeV/c and suggest that the spectrum has an increasing inverse slope from ≈0.2 to 0.4 GeV/c with increasing p_T, which indicates a possible sensitivity of the measurement to photons from earlier stages of the evolution of the collision. In addition, like the direct-photon production, the p_T-integrated nonprompt direct-photon yields also follow a power-law scaling behavior as a function of collision-system size. The exponent, α, for the nonprompt component is found to be consistent with 1.1 with no apparent p_T dependence.

DOI: 10.1103/PhysRevC.109.044912

I. INTRODUCTION

Direct photons, defined as those not coming from hadron decays, have long been considered a golden probe towards our understanding of the evolution of relativistic heavy-ion collisions, from the quark-gluon plasma (QGP) phase to the hadron-gas (HG) phase [1]. Unlike strongly interacting probes, such as identified particles and jets, direct photons traverse the medium unmodified due to the small cross section of electromagnetic interaction. These penetrating photons encode information about the environment in which they were created, including the temperature and the collective motion of the medium. While the direct photons at high transverse momentum, p_T, are dominated by photons created from hard-scattering processes, such as quark-gluon Compton scattering, in the low-p_T regime, they were initially predicted to be of a thermal origin, being emitted from the QGP and HG phase (see Ref. [2] for a recent review).

The p_T spectrum of low-p_T direct photons from Au+Au collisions at $\sqrt{s_{NN}} = 200$ GeV, first measured by PHENIX [3], shows a clear excess above the hard-scattering contribution estimated from $p+p$ measurements for p_T below 3 GeV/c. Followup measurements by PHENIX have established that low-p_T direct-photon emission also shows a large anisotropy with respect to the reaction plane [4,5], and that the yield increases faster than $N_{\rm part}$ or $dN_{\rm ch}/d\eta$ as a function of the centrality of the collision [6]. Low-p_T direct photons in Au+Au collisions at 200 GeV have also been measured by STAR [7] using the same basic method as [3], but different detection techniques, which leads to different systematic uncertainties between STAR and PHENIX measurements. Quantitatively, STAR results appear to be a factor 3 smaller than those from PHENIX. This tension has not yet been resolved. Furthermore, low-p_T photons have been measured in Au+Au at lower $\sqrt{s_{NN}}$ of 39 and 62.9 GeV by PHENIX [8], and in Pb+Pb at $\sqrt{s_{NN}} = 2760$ GeV by ALICE [9].

The excess of direct photons in $A+A$ collisions, in the low-p_T regime, is usually interpreted as the contribution of thermal radiation emitted from the expanding and cooling QGP and HG phase. Due to the rapid anisotropic expansion of the system, the radiation is Doppler shifted. Over the years, several theoretical models have been developed and refined to describe the production rates and space-time evolution of thermal photons in relativistic heavy-ion collisions [10–17]. While most of these state-of-the-art models describe the data qualitatively, they fall short of simultaneously describing all the features of the data quantitatively. To describe the large yield, early emission at high temperatures is favored, while sufficient buildup of collective motion is required to explain the large anisotropy, thereby favoring late-stage emission. This tension, often termed the "direct-photon puzzle," hints at an incomplete understanding of the different sources and mechanisms of direct-photon production. This has triggered more thoughts on other unconventional photon sources, such as emission from the preequilibrium stage, strong magnetic field effects, etc. [10,18–24]. For that very reason this paper refers to the low-p_T-excess direct photons as "nonprompt" instead of "thermal."

To provide new insights and further understandings, the PHENIX Collaboration presents results from the high-statistics 2014 Au + Au data at $\sqrt{s_{NN}} = 200$ GeV. With a tenfold increase in statistics compared to previously published

results, differential direct-photon measurements as functions of p_T and system size over a broad p_T range from 0.8 to 10 GeV/c and in 10% centrality classes are discussed. A new algorithm, which utilizes the silicon-vertex detector (VTX) as the conversion material for photons, is developed for this analysis.

The paper is organized as follows: Section II presents the experimental setup relevant to this measurement and the algorithm to reconstruct the conversion photons. Section III describes the double-ratio method to determine the direct-photon excess ratio, R_γ, and gives details of the experimental measurement. Section IV investigates the systematic uncertainties. Section V discusses the results. Section VI presents the summary and conclusions. Finally, there are two Appendixes: Appendix A discusses the event mixing procedures and their validity, while Appendix B describes the Monte Carlo (MC) sampling method used to derive the final systematic uncertainties on the direct-photon yield.

II. EXPERIMENTAL SETUP AND PHOTON MEASUREMENTS

A. PHENIX 2014 Au+Au $\sqrt{s_{NN}} = 200$ GeV data set

In 2014, a total of 1.9×10^{10} Au+Au collisions at $\sqrt{s_{NN}} =$ 200 GeV were recorded by the PHENIX detector at the Relativistic Heavy Ion Collider (RHIC) with a minimum-bias (MB) trigger, based on the response of two beam-beam counters (BBCs) [25]. The BBCs are located on either side of the interaction point along the beam axis at $z = \pm1.44$ m with a pseudorapidity coverage of $3.1 < |\eta| < 3.9$ and full 2π azimuthal acceptance. The MB trigger requires a coincident signal in both BBCs. Each BBC, comprising 64 Čerenkov counters, measures the total number of charged particles produced during the collision within its acceptance. The charged-particle multiplicity is used to divide the MB events into different centrality classes; 0%–10% corresponds to the most central collisions which produces the largest number of charged particles, while 80%–93% corresponds to peripheral collisions with only a small number of charged particles. The BBCs also utilize the arrival time of the produced particles on each side to determine the collision vertex along the beam direction.

The direct-photon measurement presented here is based on the tracking and identification of electrons and positrons from photon conversions in the detector material and the direct calorimetric measurement of photons in the two PHENIX central arm spectrometers shown in Fig. 1 [26]. The VTX [27] comprises four silicon layers at nominal radii of 2.6, 5.1, 11.8, and 16.7 cm. In the beam direction, the active area covers approximately ±11 cm for the innermost layer and ±19 cm for the outer layer. The VTX is not used as an active detector in the measurement. However, it acts as the photon converter, which is critical for this analysis. The total material thickness of the VTX in terms of radiation length, X_0, is $\approx13\%X_0$. Events are selected with a z vertex within ±10 cm of the nominal interaction point. After applying quality assurance criteria, a total of 1.25×10^{10} events are analyzed.

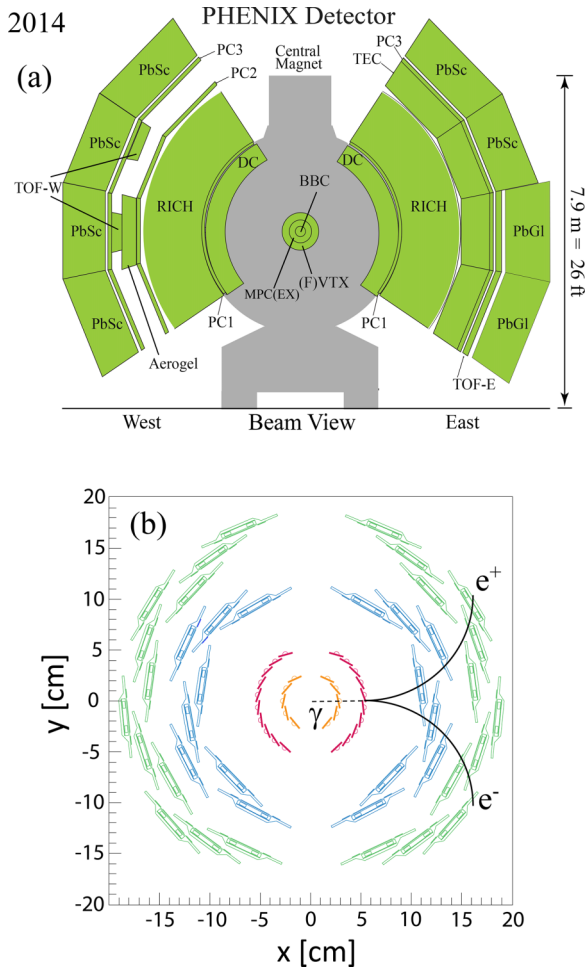

FIG. 1. (a) The beam view of the PHENIX central-arm spectrometer for the year 2014. (b) A magnified view of the silicon-vertex detector. The solid curves correspond to the electron and positron tracks from photon conversion.

The central-arm spectrometers have three major parts: A charged-particle tracking system [28,29], particle-identification detectors [30], and electromagnetic calorimeters (EMCal) [31]. Each arm covers 90° in the azimuthal direction with $|\eta| < 0.35$. The tracking system is located ≈2.2 m from the beam axis outside of an axial magnetic field. The main tracking detectors are drift chambers (DC) and pad chambers (PC1). The DC provides a precise measurement of the transverse momentum for charged particles with $p_T > 0.2$ GeV/c. The PC1 measures the momentum along beam direction, p_z. The effective momentum resolution of the central-arm tracking system, for this analysis, is $\sigma_p/p = 0.8\%\oplus2\%\,p$ [GeV/c], where p is the transverse momentum of the track.

Charged tracks are identified as electrons or positrons with a ring-imaging Čerenkov detector (RICH). The RICH has a CO_2 gas radiator with a low radiation threshold for electrons (0.018 GeV/c) and a relatively high threshold for charged pions (>4.87 GeV/c). Requiring a signal in at least two phototubes in the focal plane of the RICH at the expected ring location effectively separates electrons below 5 GeV/c

from charged hadrons. A further matching of the momentum, p, of the charged track to the energy, E, as measured in the EMCal within $-2\sigma_{E/p} < E/p < 5\sigma_{E/p}$ removes most hadrons remaining in the sample. Here $\sigma_{E/p}$ is the momentum-dependent resolution of the energy to momentum ratio, E/p.

For the calorimetric identification of photons, two types of calorimeters are used, lead-scintillator (PbSc) and lead-glass (PbGl). The PbSc EMCal, which covers 3/4 of the acceptance, is a sandwich sampling detector, also referred to as a Shashlik type calorimeter. Based on the widths of reconstructed π^0 mass through the $\pi^0 \to \gamma\gamma$ decay, the effective photon-energy resolution in this analysis is $\sigma_E/E = 8.1\%/\sqrt{E\,[\mathrm{GeV}]} \oplus 5.0\%$. The remaining 1/4 of the acceptance is covered by the PbGl EMCal, which is a homogeneous Čerenkov-type detector with an effective resolution of $\sigma_E/E = 8.7\%/\sqrt{E\,[\mathrm{GeV}]} \oplus 5.8\%$. Nominal cuts on the energy threshold ($E > 500$ MeV) and shower shape ($\chi^2 < 3$) are applied to identify photons.

B. External photon conversions in the VTX

Earlier measurements of direct photons from PHENIX are based on three different strategies to measure photons in $A+A$ collisions. The calorimeter method is used to measure photons with p_T of several GeV/c via their energy deposited in the EMCal [4]. To access lower p_T, e^+e^- pairs from photon conversions are reconstructed with the tracking system. These e^+e^- pairs are either from "internal" conversions of virtual photons emitted from the collision [3] or "external" conversions of photons in the detector material [6].

Here, external photon conversions at the VTX detector are reconstructed from e^+e^- pairs. The VTX material is distributed between 2 and 25 cm along the radial direction. Depending on the conversion point, a different amount of magnetic field is traversed by the e^+e^- pair. In the standard PHENIX track-reconstruction algorithm, the tracking system measures a part of the trajectory outside of the magnetic field at a radial position of ≈2.2 m. The momentum vector is determined by assuming that the particle originates at the event vertex. This assumption is incorrect for the e^+e^- pairs from conversions in the VTX material. Both e^+ and e^- traverse a smaller $\int B\,dl$ than tracks from the vertex, and thus the azimuthal component of the momentum vector is mismeasured in opposing directions, leading to an artificial opening angle and mismeasured mass of the e^+e^- pair. Because the magnetic field in the region of the VTX detector is approximately constant at 0.9 T, the artificial mass acquired is proportional to the radial location of the conversion point. Figure 2 shows the mass of e^+e^- pairs simulated with the GEANT3 PHENIX-detector simulation [32]; different curves represent photon conversions in different VTX layers. The $m_{e^+e^-}$ is larger for conversions at larger radii, with most conversions occurring in the third and fourth layers of the VTX, where the material budget is the largest.

To correctly reconstruct and identify photon conversions at different VTX layers, a new track-reconstruction algorithm is developed. The new algorithm relies on the fact that the e^+ and e^- from a conversion have the same origin and that their momenta were initially parallel in radial direction. This additional constraint eliminates the need to assume the origin of the track.

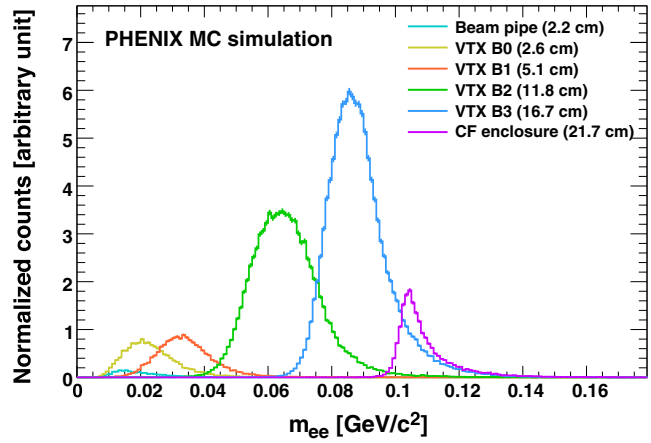

FIG. 2. Artificial e^+e^- pair mass for external photon conversions. Each curve corresponds to a different radius region, which roughly maps to the locations of beam pipe, layers 1 (B0) through 4 (B3) of the VTX, and the VTX (CF) carbon-fiber enclosure.

The algorithm is illustrated in Fig. 3. For all radii between 0 and 30 cm, all possible momenta of the e^+ and e^- are scanned to identify the azimuthal location $\phi_\pm$ at which the track is perpendicular to the circle of the given radius, or in other words points back radially to the event vertex. The conversion point is determined by finding the radius for which the difference of the azimuthal angles of the e^+e^- pair, $\delta\phi = \phi_+ - \phi_-$, becomes zero. If such radius exists, the pair is identified as a

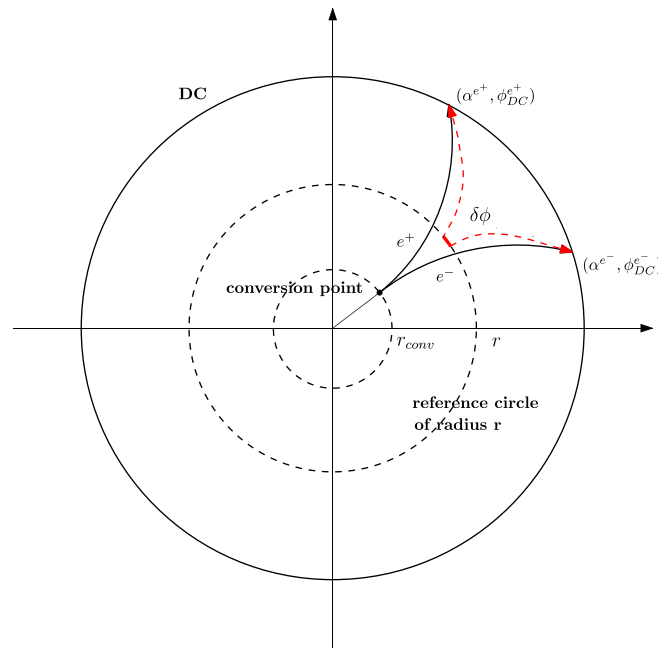

FIG. 3. Schematic view of the conversion-reconstruction algorithm. The two tracks are reconstructed to the same radius r. $\delta\phi$ is the azimuthal-angular difference between the two tracks for a given reconstruction radius. $\delta\phi$ is zero at the conversion point.

conversion candidate at the location ($\phi_{\rm conv}$, $r_{\rm conv}$), where $\phi_{\rm conv}$ is the azimuthal angle of the conversion point, reconstructed with a resolution of ≈4 mrad, and $r_{\rm conv}$ is the radial position reconstructed with a resolution of ≈2 cm.

III. DATA ANALYSIS

A. Double-ratio tagging method

The number of direct photons emitted in a Au+Au collision is small compared to the number of photons from hadron decays. To make a precise measurement of the direct-photon yield, a tagging method is employed [6], which measures the ratio, R_γ, of all photons, referred to as inclusive photons, $\gamma^{\rm incl}$, to the photons from hadron decays, $\gamma^{\rm hadr}$. The ratio R_γ is evaluated as double ratio, such that most systematic uncertainties cancel explicitly. The R_γ given in Eq. (1) features three main terms:

$$R_\gamma = \frac{\gamma^{\rm incl}}{\gamma^{\rm hadr}} = \frac{\left(\frac{\gamma^{\rm incl}}{\gamma^{\pi^0}}\right)}{\left(\frac{\gamma^{\rm hadr}}{\gamma^{\pi^0}}\right)} = \frac{\langle \epsilon_\gamma f \rangle \left(\frac{N_\gamma^{\rm incl}}{N_\gamma^{\pi^0,{\rm tag}}}\right)_{\rm Data}}{\left(\frac{\gamma^{\rm hadr}}{\gamma^{\pi^0}}\right)_{\rm Sim}}. \tag{1}$$

(i) The ratio of measured photon yields $N_\gamma^{\rm incl}/N_\gamma^{\pi^0,{\rm tag}}$ is the number of measured conversion photons in a given p_T bin, divided by the subsample of those conversion photons that are tagged by a second photon as resulting from a $\pi^0 \to \gamma\gamma$ decay. This quantity is measured in bins of fixed conversion photon p_T.

(ii) The conditional acceptance and efficiency $\langle \epsilon_\gamma f \rangle$ is the conditional probability to detect and reconstruct the second π^0 decay photon with the EMCal, given that the first decay photon was reconstructed as e^+e^- pair from a photon conversion. The probability is averaged over all parent π^0 p_T that can contribute to the given conversion photon p_T.

(iii) The cocktail ratio $\gamma^{\rm hadr}/\gamma^{\pi^0}$ is the ratio of all photons from hadron decays over only those photons from π^0 decays.

The following sections discuss how each term is determined.

B. Ratio of the measured photon yields $N_\gamma^{\rm incl}/N_\gamma^{\pi^0,{\rm tag}}$

Electrons and positrons in a given event are combined to e^+e^- pairs and conversion candidates are selected with appropriate cuts, which results in a foreground sample of e^+e^- pair FG$^{\rm ee}$. All conversion candidates in a conversion photon p_T bin, are combined with all photon showers in the EMCal above an energy threshold, $E_{\rm cut}$. The invariant mass $m_{ee\gamma}$ is calculated and all combinations that lie in a mass window around the π^0 mass are considered as candidates for tagged photons FG$^{ee\gamma}$. Due to the large particle multiplicity in Au+Au collisions, there are many false combinations where the electron, positron, or photon are not from the same source. These background pairs must be subtracted statistically to obtain the signals of interest SG$^{\rm ee}$ and SG$^{ee\gamma}$.

For e^+e^- pairs, there are two possible combinations, signal pairs of interest SG$^{\rm ee}$ and uncorrelated background BG$^{\rm ee}$ pairs where the electron and positron are from different sources. Their sum constitutes the foreground FG$^{\rm ee}$:

$$\mathrm{FG}^{\rm ee} = \mathrm{SG}^{\rm ee} + \mathrm{BG}^{\rm ee}. \tag{2}$$

When the e^+e^- pairs are combined with photons to $e^+e^-\gamma$ combinations, both types of e^+e^- pairs are combined with photons that are either correlated or uncorrelated with the pair:

$$\mathrm{FG}^{ee\gamma} = \mathrm{SG}^{ee\gamma} + \mathrm{BG}^{ee\gamma}_{\rm uncorr} + \mathrm{BG}^{ee\gamma}_{\rm corr}. \tag{3}$$

Introducing i, j, k as the source of the positron, electron, and photon, respectively, the terms in Eq. (3) are the following:

(1) The first term is the signal of interest with positron, electron, and photon from the same source ($i = j = k$).

(2) The second term represents the cases where the e^+e^- pair is combined with uncorrelated photons. This includes the case ($i = j \neq k$), where the e^+e^- pair is correlated and randomly combined with a γ, as well as the case ($i \neq j \neq k$), where all three are from different sources.

(3) The third term represents cases $[(i \neq j = k) \vee (j \neq i = k)]$, where the e^+e^- pair is not from the same source but the γ is correlated with either the e^+ or the e^-.

Each of the background terms is determined with different event-mixing procedures, which were developed using the MC method. The event-mixing procedures and their validity are discussed in detail in Appendix A.

1. Determination of the inclusive photon yield $N_\gamma^{\rm incl}$

Photons that convert at the VTX detector are selected by pairing electron and positron tracks to e^+e^- pairs. All pairs are required to have a valid conversion point at a radial location within the VTX detector, between 1 and 29 cm. In addition, both tracks need to match in the beam direction within $|\Delta z| < 4$ cm. The invariant mass distribution of the selected e^+e^- conversion pairs is shown in Fig. 4 for the p_T range $1.0 < p_T < 1.2$ GeV/c. The four panels correspond to four different centrality selections. Each panel shows the same peak structure, which is characteristic of the multilayer structure of the VTX detector.

The e^+e^- pairs passing the conversion selection criteria contain uncorrelated e^+e^- pairs, where the e^+ and e^- are from different sources. These backgrounds are also shown in Fig. 4. Because of its combinatorial nature, the background to foreground ratio increases towards more central-event selections. An event-mixing technique is used to estimate and subtract this background (see Appendix A for details). In this technique, an e^+ from event A is paired with an e^- from another event B to produce the random e^+e^- pair sample. To assure the events A and B have similar topological characteristics, it is required that both events

(a) are from the same 10% centrality selection,
(b) have their interaction vertex within $\Delta z = 2.5$ cm,
(c) have their reaction planes aligned within $\Delta\phi = \pi/6$.

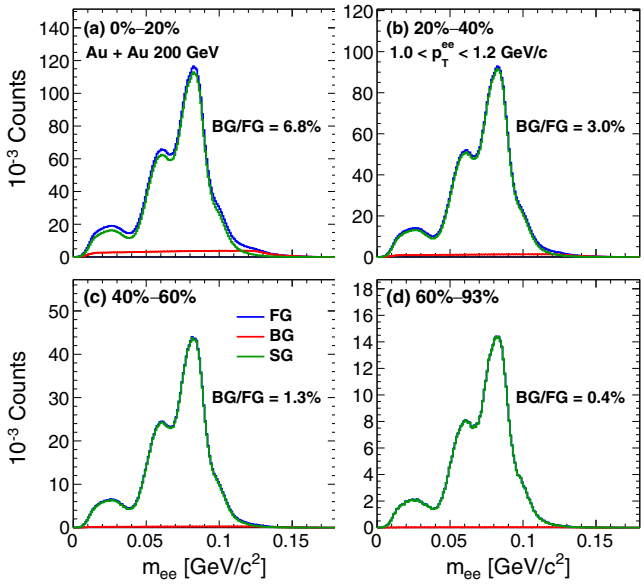

FIG. 4. Mass distribution, $m_{e^+e^-}$, of the e^+e^- pairs after conversion selection cuts are applied. All four panels are for the same p_T range $1.0 < p_T < 1.2$ GeV/c for four different centrality selections (a) 0%–20%, (b) 20%–40%, (c) 40%–60%, and (d) 60%–93%. Shown are the foreground $\mathrm{FG}^{\mathrm{ee}}$, background $\mathrm{BG}^{\mathrm{ee}}$, and signal $\mathrm{SG}^{\mathrm{ee}}$.

After the subtraction of the uncorrelated background, more than 99% of the pairs are from photon conversion in the VTX materials. The remaining pairs are from internal virtual photon conversions that passed the conversion selection criteria. The sources of these pairs are similar to those of the photon conversion pairs, with the majority resulting from π^0 Dalitz decays. An additional lower mass cut at 0.04 GeV/c^2 removes about 90% of theses internal conversions, rendering the remainder negligible. Finally, N_γ^{incl} is calculated by integrating the counts in the mass range from 0.04 to 0.12 GeV/c^2, corresponding to layers 3 and 4 of the VTX. The analysis is repeated for bins in p_T and in centrality.

2. *Tagged photon raw yield* $N_\gamma^{\pi^0,\mathrm{tag}}$

Next, the subset of e^+e^- pairs in the N_γ^{incl} sample that can be tagged as photons from a π^0 decay, $N_\gamma^{\pi^0,\mathrm{tag}}$, is determined. For a given event, each e^+e^- conversion candidate, in the mass window in which N_γ^{incl} is counted, is paired with all reconstructed showers in the EMCal with shower shape $\chi^2 < 3$ and energy larger than $E_{\mathrm{cut}} = 0.5$ GeV, excluding those matched to the e^+e^- pair itself. The energy cut, together with the p_T cut of 0.2 GeV/c on the e^+ and e^-, constitutes an implicit asymmetry cut on the π^0 decay photons that depends on the p_T of the π^0. For all $e^+e^-\gamma$ combinations, the invariant mass $m_{ee\gamma}$ is calculated. This constitutes the foreground $\mathrm{FG}^{ee\gamma}$, for which an example is given in Fig. 5 for the e^+e^- pair in the p_T range $1.0 < p_T < 1.2$ GeV/c. The four panels (a) to (d) correspond to four centrality selections 0%–20%, 20%–40%, 40%–60%, and 60%–93%, respectively.

Despite the large background, the signal, $\mathrm{SG}^{ee\gamma}$, is clearly visible as a peak around the π^0 mass, even in panel (a), which is the most central event selection. As discussed above, the background $\mathrm{BG}^{ee\gamma}$ has two components:

$$\mathrm{BG}^{ee\gamma} = \mathrm{BG}^{ee\gamma}_{\mathrm{uncorr}} + \mathrm{BG}^{ee\gamma}_{\mathrm{corr}}, \tag{4}$$

for which the shape and normalization are obtained from the event-mixing procedures described in Appendix A. The results are also shown in Fig. 5. The uncorrelated background, $\mathrm{BG}^{ee\gamma}_{\mathrm{uncorr}}$, is given in panels (a) to (d). The much smaller correlated background, $\mathrm{BG}^{ee\gamma}_{\mathrm{corr}}$, is only revealed after $\mathrm{BG}^{ee\gamma}_{\mathrm{uncorr}}$

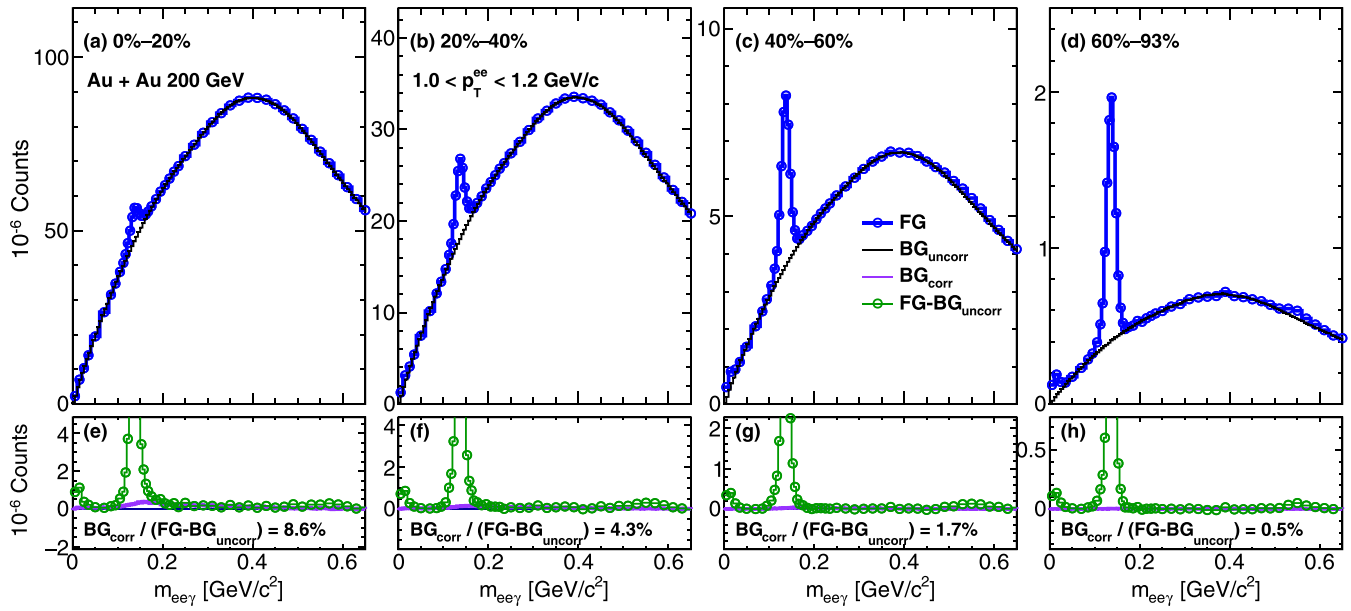

FIG. 5. Mass distribution, $m_{ee\gamma}$, for e^+e^- pairs with p_T from 1.0 to 1.2 GeV/c, for four centrality selection (a), (e) 0%–20%, (b), (f) 20%–40% (c), (g) 40%–60%, and (d), (h) 60%–93%. Panels (a) through (d) show the foreground $\mathrm{FG}^{ee\gamma}$ and the uncorrelated background $\mathrm{BG}^{ee\gamma}_{\mathrm{uncorr}}$. Panels (e) through (h) show the difference $\mathrm{FG}^{ee\gamma} - \mathrm{BG}^{ee\gamma}_{\mathrm{uncorr}}$, together with the correlated background $\mathrm{BG}^{ee\gamma}_{\mathrm{corr}}$.

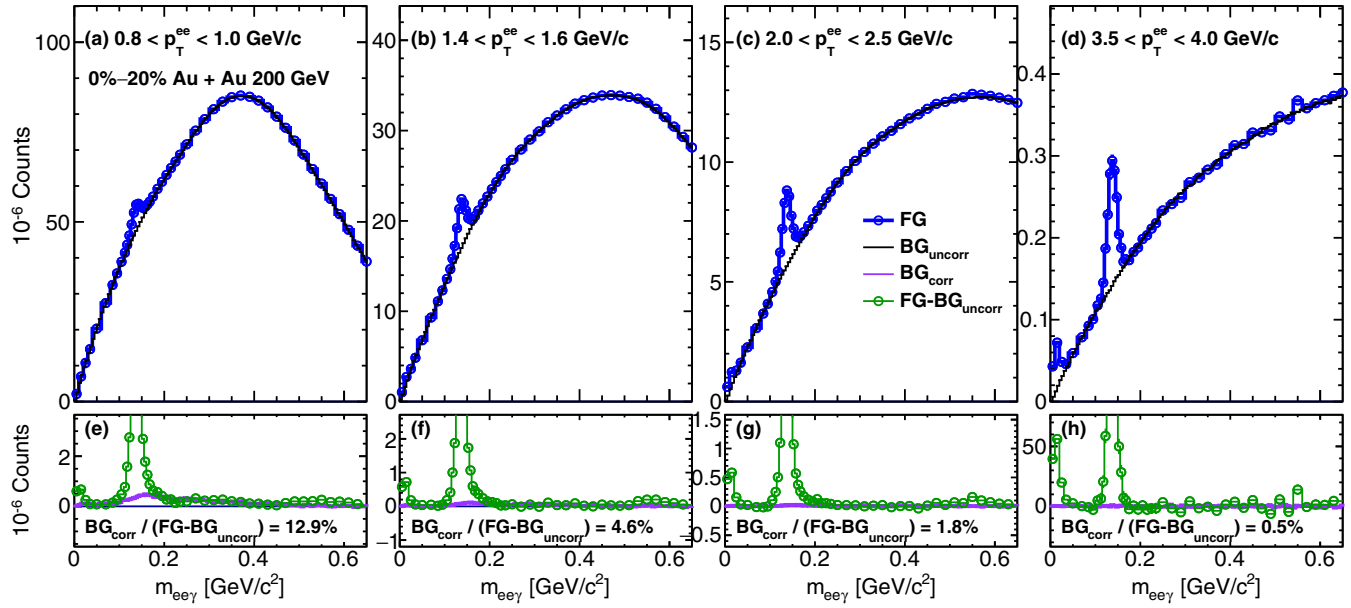

FIG. 6. Mass distribution, $m_{ee\gamma}$, for e^+e^- pairs from the 0%–20% centrality selection for four different e^+e^- pair p_T regions, (a), (e) 0.8 to 1.0, (b), (f) 1.4 to 1.6, (c), (g) 2.0 to 2.5, and (d), (h) 3.5 to 4 GeV/c. Panels (a) through (d) show the foreground $\mathrm{FG}^{ee\gamma}$ and the uncorrelated background $\mathrm{BG}^{ee\gamma}_{\mathrm{uncorr}}$. Panels (e) through (h) show the difference $\mathrm{FG}^{ee\gamma} - \mathrm{BG}^{ee\gamma}_{\mathrm{uncorr}}$, together with the correlated background $\mathrm{BG}^{ee\gamma}_{\mathrm{corr}}$.

is subtracted from the foreground, $\mathrm{FG}^{ee\gamma}$. The differences are given in panels (e) to (h) for central to peripheral events, respectively. Figure 5 indicates that the correlated background decreases with centrality from $\mathrm{BG}^{ee\gamma}_{\mathrm{corr}}/(\mathrm{FG}^{ee\gamma} - \mathrm{BG}^{ee\gamma}_{\mathrm{uncorr}}) = 8.6\%$ in central collisions to 0.5% in the most-peripheral collisions.

For the 0%–20% centrality selection, Fig. 6 shows the mass distributions $m_{ee\gamma}$ for four different e^+e^- pair p_T ranges. The representation is the same as for Fig. 5. Panels (a) through (d) all show a clear peak around the π^0 mass. The backgrounds are the largest for low p_T and the most central events. As p_T increases and the event multiplicity decreases, the backgrounds are significantly reduced. Because of the complexity of the particle correlations present in the real Au + Au collision events, including effects of collective expansion, jet production, hadron decays, etc., there is a small residual background that is not captured by the event-mixing procedure. To remove this background, a low-order polynomial, $f_{ee\gamma}$, is fitted to the ratio $(\mathrm{FG}^{ee\gamma} - \mathrm{BG}^{ee\gamma})/\mathrm{BG}^{ee\gamma}_{\mathrm{uncorr}}$ in the mass range 0.05–0.08 and 0.23–0.45 GeV/c^2. This function is used to correct $\mathrm{BG}^{ee\gamma}_{\mathrm{uncorr}}$ before it is finally subtracted. Thus, the final distribution for $N_\gamma^{\pi^0,\mathrm{tag}}$ is

$$N_\gamma^{\pi^0,\mathrm{tag}} = \mathrm{FG}^{ee\gamma} - \mathrm{BG}^{ee\gamma}_{\mathrm{corr}} - (1 + f_{ee\gamma}) \times \mathrm{BG}^{ee\gamma}_{\mathrm{uncorr}}. \quad (5)$$

An example of the residual background is given in Fig. 7 for the e^+e^- pair p_T range of 1 to 1.2 GeV/c and 0%–20% centrality selection. In panel (a), $\mathrm{FG}^{ee\gamma}$ with all the background components are shown. Panel (b) gives a second-order polynomial fit to the ratio $(\mathrm{FG}^{ee\gamma} - \mathrm{BG}^{ee\gamma})/\mathrm{BG}^{ee\gamma}_{\mathrm{uncorr}}$ ratio, $f_{ee\gamma}$, which is used to determine the residual background. Due to the unfavorably small signal-to-background ratio in this case, the residual background in the π^0 mass region is ≈9.4%. The residual background quickly drops with p_T and centrality bins, for example as p_T increases to 3 GeV/c, the residual background reduces to 2.7%. For each p_T-centrality bin combination, $N_\gamma^{\pi^0,\mathrm{tag}}$ is extracted by integrating the number of

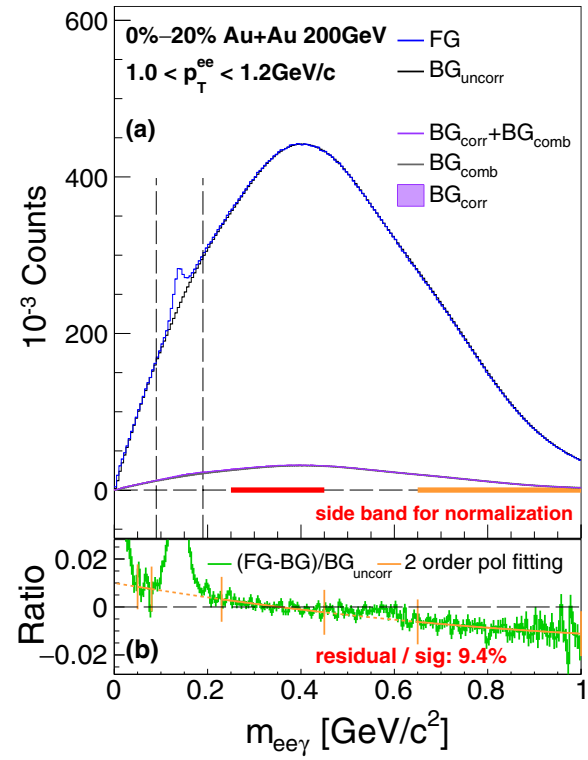

FIG. 7. (a) An example for $\mathrm{FG}^{ee\gamma}$ and the various background components after normalization in the indicated regions. (b) The ratio $(\mathrm{FG}^{ee\gamma} - \mathrm{BG}^{ee\gamma})/\mathrm{BG}^{ee\gamma}_{\mathrm{uncorr}}$ and the polynomial fit to determine the residual-background correction $f_{ee\gamma}$.

entries in a window around the π^0 peak ($0.09 < m_{ee\gamma} < 0.19$) GeV/$c^2$ after all background subtractions are applied.

Note that the extracted $N_\gamma^{\pi^0,\mathrm{tag}}$ described in the this section can also be used to measure the π^0 invariant yield once corrected with detector acceptance and efficiency, which can potentially extend the previous PHENIX π^0 measurements [33] to lower p_T regions. However, to establish such a measurement, in particular the evaluation of systematic uncertainties requires significant additional work that is beyond the scope of this paper.

C. Conditional probability $\langle \epsilon_\gamma f \rangle$

The probability, $\langle \epsilon_\gamma f \rangle$, that the second photon is in the acceptance and is reconstructed, given a conversion e^+e^- pair from a π^0 decay, is extracted from the single π^0 simulation. In this simulation, individual π^0 are tracked through the PHENIX MC-simulation framework. The π^0 are generated with $d^2N/dp_T dy$ spectra that were fitted to $\pi^\pm$ and π^0 data measured by PHENIX (see Sec. III D), uniform in the rapidity range $|y| < 0.5$, and uniform over 2π in azimuthal angle, ϕ.

The energy scale and resolution of the EMCal in the MC simulation is tuned as closely as possible to resemble the one observed in data by comparing the mean and width of the measured and simulated π^0 mass distribution. The π^0 are reconstructed through the $\pi^0 \to \gamma\gamma$ decay channel. For this purpose an asymmetry of less than 20% between the energies of the two decay photons was applied to keep the two-photon energies similar.

In the single π^0 MC simulation, e^+e^- pairs in the mass window $0.04 < m_{e^+e^-} < 0.12$ GeV/c^2 are counted to determine $N_{ee}^{\pi^0}$, the number of reconstructed e^+e^- pairs in a given e^+e^- pair p_T bin. The subsample for which the second photon of the π^0 decay is reconstructed as a shower in the EMCal is counted as $N_{ee}^{\pi^0,\mathrm{tag}}$. The value of $\langle \epsilon_\gamma f \rangle$ is then determined as

$$\langle \epsilon_\gamma f \rangle = \frac{N_{ee}^{\pi^0,\mathrm{tag}}}{N_{ee}^{\pi^0}}. \tag{6}$$

For the extraction of $N_{ee}^{\pi^0,\mathrm{tag}}$ the presence of other showers in the EMCal needs to be taken into account. This is done by embedding the showers from the simulated single π^0 into the EMCal response from Au+Au collisions at the tower level. The combined EMCal information is then reclustered to form new showers. All of the showers that contain energy deposited by the embedded singe π^0 (identified by the MC ancestry information) are combined with the e^+e^- pair.

Similar to the $N_\gamma^{\pi^0,\mathrm{tag}}$ extraction from data, a residual background subtraction is applied. This eliminates any remaining background inside the π^0 counting window. The residual background is estimated by a second-order polynomial function fit in the mass range 0.05–0.08 and 0.23–0.45 GeV/c^2. This residual background mainly comes from events where both decay photon convert to e^+e^- pairs, and the reconstructed conversion photon gets paired with the EMCal cluster of the e^+ or e^- from the other conversion. The extracted $\langle \epsilon_\gamma f \rangle$ is shown in Fig. 8 as a function of the e^+e^- pair p_T for the four centrality selections.

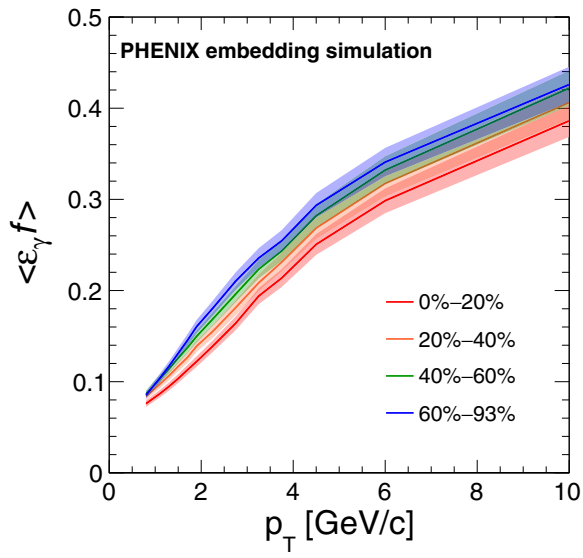

FIG. 8. Conditional probability $\langle \epsilon_\gamma f \rangle$ as a function of p_T in 0%–20%, 20%–40%, 40%–60%, and 60%–93% centrality classes.

The increasing trend of $\langle \epsilon_\gamma f \rangle$ with increasing conversion photon p_T is partly due to the decrease in the opening angle between the conversion photon and the second photon so that the second photon is more likely to fall into the acceptance of the EMCal. Another important factor is that the average energy of the second photon increases with increasing conversion photon p_T, and hence the efficiency of the energy threshold cut increases towards higher p_T. The difference in $\langle \epsilon_\gamma f \rangle$ between different centrality classes is mainly related to the shower shape (χ^2) selection, because the showers are more distorted in central Au + Au collisions due to the larger detector occupancy, resulting in more accidental overlaps from the underlying event, and the centrality dependent parent π^0 p_T distributions.

D. Cocktail ratio $\gamma^{\mathrm{hadr}}/\gamma^{\pi^0}$

The last ingredient to calculate R_γ is the cocktail ratio $\gamma^{\mathrm{hadr}}/\gamma^{\pi^0}$ of photons from π^0, η, ω, and η' decays over those from π^0 decays. The cocktail ratio is obtained using the PHENIX meson decay generator EXODUS, which simulates mesons according to given input p_T spectra, decays them based on the known decay kinematics and branching ratios, and aggregates the decay photons in the PHENIX detector acceptance.

The photons from π^0 decays are generated from distributions obtained by fitting a modified Hagedorn function [Eq. (7)] to charged pion [34] and neutral pion [33,35] data measured by PHENIX for the rapidity range $|y| < 0.5$:

$$E\frac{d^3N_\pi^0}{dp^3} = A\left(e^{-(ap_T+bp_T^2)} + \frac{p_T}{p_0}\right)^{-n}. \tag{7}$$

The fit parameters are summarized in Table I for MB collisions, as well as for nine centrality bins. The η meson p_T spectra are obtained by multiplying the π^0 spectrum with the

TABLE I. Parameters for the modified Hagedorn function Eq. (7) to PHENIX data [33–35] from Au+Au collisions at $\sqrt{s_{NN}} = 200$ GeV.

Centrality	A $[(\mathrm{GeV}/c)^{-2}]$	a $[(\mathrm{GeV}/c)^{-1}]$	b $[(\mathrm{GeV}/c)^{-2}]$	p_0 (GeV/c)	n
min. bias	504.5	0.5169	0.1626	0.7366	8.274
0%–10%	1331.0	0.5654	0.1945	0.7429	8.361
10%–20%	1001.0	0.5260	0.1628	0.7511	8.348
20%–30%	750.7	0.4900	0.1506	0.7478	8.229
30%–40%	535.3	0.4534	0.1325	0.7525	8.333
40%–50%	364.5	0.4333	0.1221	0.7385	8.261
50%–60%	231.2	0.4220	0.1027	0.7258	8.220
60%–70%	118.1	0.4416	0.0559	0.7230	8.163
70%–80%	69.2	0.2850	0.0347	0.7787	8.532
80%–93%	51.1	0.2470	0.0619	0.7101	8.453

η/π^0 ratio, following the procedure suggested in [36]:

$$E\frac{d^3N_\eta}{dp^3} = E\frac{d^3N_\pi^0}{dp^3} \times \eta/\pi^0 \times R_{\mathrm{flow}}, \tag{8}$$

where R_{flow} is the ratio of $K^\pm/\pi^\pm$ for a given centrality over $K^\pm/\pi^\pm$ in $p+p$ collisions. This procedure makes use of the world data for η/π^0 from $p+p$ and small system collisions (see [36] for references), and it avoids the assumption of m_T scaling used in earlier work [6], which has been shown to overestimate the number of η mesons produced below 2 GeV/c in p_T in $p+p$ and small system collisions. It also includes the centrality dependent modification, R_{flow}, of the η p_T spectra in Au+Au collision due to radial flow, which was not taken into account in earlier work [6]. The modification R_{flow} is estimated using measured kaon spectra [37]. For peripheral Au+Au collisions, the new approach to determine the η yield results in a few percent reduction of the number of predicted decay photons in the range 1–2 GeV/c, compared to the m_T scaling approach based on Eq. (7) that was taken in earlier work [6]. The difference is within the systematic uncertainties quoted in that work. For central and semicentral collisions the new and old approach agree better in the sense that they predict very similar decay photon yields above 1 GeV/c, with any differences being much smaller than the quoted systematic uncertainties. This agreement arises when accounting for the modification of the η meson spectrum due to radial flow, which shifts η mesons from low to mid p_T. This shift results in more decay photons above 1 GeV/c in the presence of radial flow, and moving the predicted yield closer to the one derived from m_T scaling. At high p_T, the η/π^0 ratio demonstrates a universal value at high p_T, consistent with 0.487 ± 0.024, independent of collision energy, system size, or centrality. The values for dN/dy for η/π^0, $K^\pm/\pi^\pm$ and R_{flow} are summarized in Table II for $1.0 < p_T < 2.0$ GeV/c, where the effects of flow are expected to be the largest for different centralities for Au+Au collisions at 200 GeV.

The contribution from ω and η' decays are based on p_T distributions using the π^0 spectrum and replacing by $f(\sqrt{p_T^2 + m_{\mathrm{meson}}^2 - m_{\pi^0}^2})$. The normalization of ω and η' are fixed at $p_T = 5$ GeV/c to 0.9 ± 0.06 and 0.25 ± 0.075, respectively [6]. The cocktail ratio $\gamma^{\mathrm{hadr}}/\gamma^{\pi^0}$ is shown in Fig. 9.

IV. SYSTEMATIC UNCERTAINTIES

This section describes the sources of systematic uncertainties for each of the three components for the calculation of R_γ. The systematic uncertainties are categorized into three types according to the correlation between the measured data points:

(i) Type A: No (or unknown) correlation between data points. Uncertainties on the individual data points can fluctuate independently, in the same way as the statistical uncertainties.
(ii) Type B: The uncertainties are correlated between data points. The fluctuation of each data point can be determined by the fluctuation of the neighboring points.
(iii) Type C: A special form of type B uncertainty. every data point fluctuates with the exact same fraction.

In the final results, Type A systematic uncertainties are combined with the statistical uncertainties, and Types B and C are combined to obtain the total systematic uncertainty.

The following subsections discuss the major individual sources contributing to the systematic uncertainties on R_γ and on the direct-photon yield. All contributions are summarized in Table III and depicted in Figs. 10 and 11 as functions of p_T for R_γ and γ^{dir}. The final systematic uncertainties on γ^{dir} and on all quantities derived from γ^{dir} are determined using the error-sampling method discussed in Appendix B

A. Systematic uncertainties on $N_\gamma^{\mathrm{incl}}/N_\gamma^{\pi^0,\mathrm{tag}}$

1. Purity of the conversion photon sample

Due to the high multiplicity of photons produced in Au+Au collisions, the background in the conversion sample

TABLE II. dN/dy for η/π^0, $K^\pm/\pi^\pm$, and R_{flow} for $1 < p_T < 2$ GeV/c for Au+Au collisions at $\sqrt{s_{NN}} = 200$ GeV. There is an overall scale uncertainty of 0.03 on $R_{\mathrm{flow}} \times (\eta/\pi^0)_{\mathrm{universal}}$.

Centrality	$K^\pm/\pi^\pm$	R_{flow}	$R_{\mathrm{flow}} \times (\eta/\pi^0)_{\mathrm{universal}}$
0%–20%	0.411 ± 0.003	1.20 ± 0.02	0.250 ± 0.004
20%–40%	0.396 ± 0.002	1.15 ± 0.02	0.237 ± 0.004
40%–60%	0.371 ± 0.002	1.08 ± 0.02	0.220 ± 0.004
60%–93%	0.337 ± 0.002	0.98 ± 0.02	0.199 ± 0.004

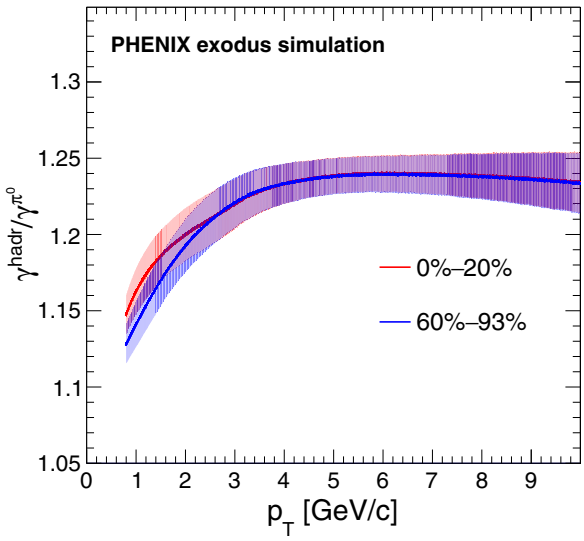

FIG. 9. Cocktail ratio as a function of p_T in the most central (0%–20%) and the most peripheral (60%–93%) centrality classes.

from uncorrelated e^+e^- pairs can be as large as 10% for the most central collisions and the lowest p_T from 0.8 to 1.0 GeV/c. This background is subtracted statistically with a certain accuracy. To estimate the effect on the final results, significantly more and less stringent conversion selection cuts were applied, hence, increasing or reducing the purity. The value of $\langle\epsilon_\gamma f\rangle\, N_\gamma^{\rm incl}/N_\gamma^{\pi^0,{\rm tag}}$, obtained from the different cuts, varies by less than 1%. This range is quoted as systematic uncertainty due to the limited purity of the conversion sample.

2. π^0 yield extraction

One of the main sources of systematic uncertainty on the R_γ measurement is the tagged photon or π^0 yield extraction. The uncertainty of π^0 yield extraction arises from two sources: (i) from the residual background subtraction, which is highly correlated with the statistical accuracy of the mixed event background normalization, and (ii) imperfect description of the large backgrounds using event-mixing techniques.

To evaluate the size of the uncertainty from the residual background subtraction, different estimates are compared. These include using different functional forms for the fit and different fit ranges to anchor the residual background fit. In addition, the counting window for π^0 signal extraction is varied. This gives a spread of $\langle\epsilon_\gamma f\rangle\, N_\gamma^{\rm incl}/N_\gamma^{\pi^0,{\rm tag}}$ values in each p_T and centrality bin. The standard deviation of the spread is quoted as the uncertainty. Due to the correlation with the statistical accuracy of the foreground in the background region, this uncertainty depends on p_T and centrality.

To test the validity of the event-mixing techniques, an MC simulation with high multiplicity π^0 events is performed. Details are discussed in Appendix A. The simulation shows that $N_\gamma^{\pi^0,{\rm tag}}/\langle\epsilon_\gamma f\rangle$ can be determined with the event-mixing technique to better than 1.5%.

B. Systematic uncertainty on $\langle\epsilon_\gamma f\rangle$

1. Energy scale

The accuracy of the energy scale of the EMCal is the main source of systematic uncertainties in the $\langle\epsilon_\gamma f\rangle$ evaluation. Because of the energy threshold cut, the second photon is reconstructed only for ≈25% of the e^+e^- pairs with the lowest p_T, even though the photon was in the EMCal acceptance. Any potential mismatch of the energy scale between the simulation and real data will cause $\langle\epsilon_\gamma f\rangle$ to be off; a higher (lower) energy scale in simulation will lead to an underestimate (overestimate) of $\langle\epsilon_\gamma f\rangle$. As mentioned earlier, to improve the accuracy, the EMCal response in the simulation is carefully tuned to the data using the π^0 mass measurement in the $\pi^0 \to \gamma\gamma$ decay channel. The tuning includes scaling the MC energy scale by 0.3% and 2.2% for the PbSc and PbGl calorimeters, respectively. In addition, the nonlinearity of the energy response is adjusted by up to 5% at the lowest measured energies. After the tuning, the π^0 peak positions in data and MC are consistent to better than 1%. Considering the additional uncertainty due to the adjustment of the nonlinearity, the energy scale is known to better than 2%. Changing the energy scale by ±2% introduces a systematic uncertainty on

TABLE III. Summary of systematic uncertainties for R_γ and $\gamma^{\rm dir}$. Uncertainties for which ranges are given vary with p_T. For details see Figs. 10 and 11.

Observable	Factor	Source	Correlation in p_T	Correlation in centrality	0%–20%	20%–40%	40%–60%	60%–93%
R_γ	$N_\gamma^{\rm incl}/N_\gamma^{\pi^0,{\rm tag}}$	$N_\gamma^{\rm incl}$ purity	Type B	Type B	<1%	<1%	<1%	<1%
		$N_\gamma^{\pi^0,{\rm tag}}$ residual background	Type A	Type A	1.5%–4.5%	0.5%–4%	0.5%–4%	0.5%–4%
		$N_\gamma^{\pi^0,{\rm tag}}$ event mixing	Type B	Type B	1.5%	1.5%	1.5%	1.5%
	$\langle\epsilon_\gamma f\rangle$	Energy scale	Type B	Type B	3%	3%	3%	3%
		Conversion loss	Type C	Type C	3%	3%	3%	3%
		γ efficiency	Type B	Type A	<1.4%	<1%	<1%	<1%
		Active area & acceptance	Type C	Type C	1%	1%	1%	1%
		Input π^0 p_T spectra	Type B	Type A	1%	1%	1%	1%
	$\gamma^{\rm hadr}/\gamma^{\pi^0}$	η/π^0	Type B	Type C	1–1.5%	1–1.5%	1–1.5%	1–1.5%
		ω, η'	Type B	Type C	<1%	<1%	<1%	<1%
	$\gamma^{\rm hadr}$	Input π^0 p_T spectrum	Type B	Type A	10%–24%	10%–24%	10%–25%	10%–24%

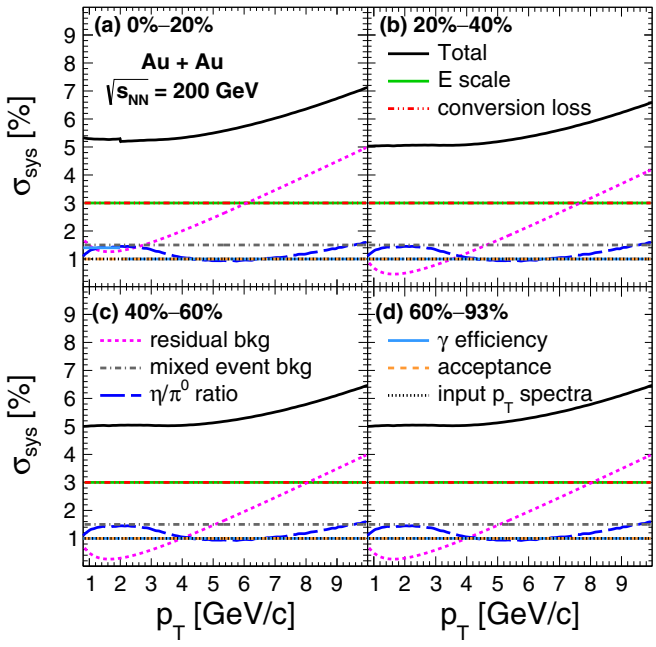

FIG. 10. Systematic uncertainties of R_γ as a function of conversion photon p_T in 0%–20%, 20%–40%, 40%–60%, and 60%–93% centrality bins. The black curve corresponds to total uncertainty, and colored curves correspond to individual sources. The lines representing uncertainties from the energy scale and the conversion loss overlap at 3%, as do the lines representing uncertainties from the γ reconstruction efficiency, acceptance, and input p_T spectra.

$\langle \epsilon_\gamma f \rangle$ of 3% at low p_T and decrease towards high p_T. The uncertainty on the energy resolution has a negligible effect.

2. Conversion photon loss

Another important source of systematic uncertainty on $\langle \epsilon_\gamma f \rangle$ is related to the probability that the second photon converts to an e^+e^- pair before reaching the EMCal. Depending on the location of the conversion point, the second photon may not be properly reconstructed, thereby reducing $\langle \epsilon_\gamma f \rangle$. To account for the "conversion loss," the material budget, i.e., thickness and location of material, implemented in the simulation framework must accurately reflect reality. If there is a mismatch, the probability for conversions to occur will be different and, hence, $\langle \epsilon_\gamma f \rangle$ will by systematically off. As there is essentially no magnetic field after the DC exit window, the e^+e^- pair from conversions between the DC and the EMCal will likely merge into one shower in the EMCal. Therefore, the value of $\langle \epsilon_\gamma f \rangle$ is most sensitive to differences in the material budget of the VTX. Comparison of the available information about the materials and their thicknesses for all detector subsystems reveals that the conversion probability in material within the magnetic field is known to better than 3%, which directly translates into and uncertainty of 3% on R_γ.

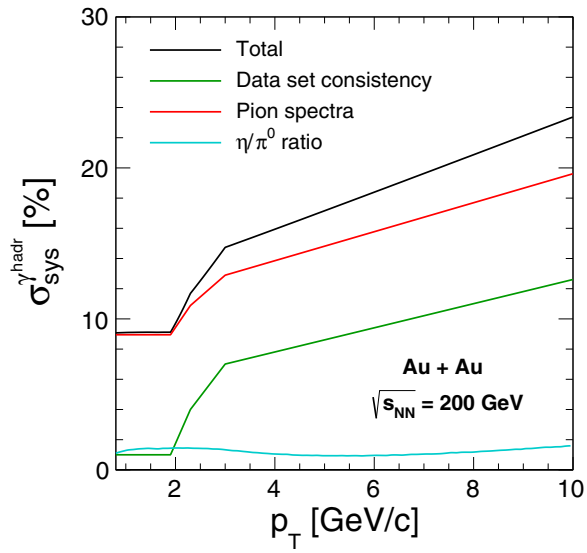

FIG. 11. Systematic uncertainties of γ^{hadr} as a function of photon p_T.

3. Photon efficiency

An EMCal shower shape, χ^2, cut is used to identify photon candidates among the EMCal energy clusters and to reduce the number of hadrons in the sample. Similar to the energy scale uncertainty, a difference between the shower shape in simulation and the data will translate directly into a systematic shift of $\langle \epsilon_\gamma f \rangle$. To evaluate this uncertainty, the χ^2 is varied simultaneously in both data and simulation and $\langle \epsilon_\gamma f \rangle$ $N_\gamma^{\text{incl}}/N_\gamma^{\pi^0,\text{tag}}$ is recalculated. It changes by 1.4% for 0.8–2 GeV/c in the 0%–20% centrality bin and by less than 1% for all the other cases.

4. Active area and geometric acceptance

Due to the limited geometrical acceptance of EMCal and some inactive areas, the second photon is registered only for ≈35% of the e^+e^- pairs at the lowest p_T. Therefore, the accuracy with which the acceptance and dead areas are known will contribute to the systematic uncertainties on $\langle \epsilon_\gamma f \rangle$. The uncertainty of the acceptance is the result of the accuracy with which the radial location of the EMCal sectors can be determined. The possible remaining offset leads to <0.3% difference in acceptance along the ϕ direction and <0.9% in the z direction. The dead areas in the real EMCal are carefully matched to the MC simulation, and the accuracy of the dead area determination is found to be better than 0.6%. It is due to the cases when a tower malfunctioned only in a very small number of events, and not masked out in the simulation. Combining all these effects, the systematic uncertainty on R_γ from the acceptance is set to 1%.

5. Input π^0 distribution

Because $\langle \epsilon_\gamma f \rangle$ is averaged over all parent π^0 p_T that contribute to a given e^+e^- pair p_T bin, the p_T dependence of $\langle \epsilon_\gamma f \rangle$ is sensitive to the shape of the π^0 distribution. The π^0 parent distribution was determined for each centrality selection by a fit to the best available data from Au+Au collisions at $\sqrt{s_{NN}} = 200$ GeV measured by the same experiment

[33–35]. The remaining uncertainty on $\langle \epsilon_\gamma f \rangle$ is smaller than 1%.

6. Weak decays and secondary interactions

The tagged photon samples include decay photons from π^0 from weak decays and π^0 produced in secondary interactions. Because these π^0 do not originate from the event vertex, $\langle \epsilon_\gamma f \rangle$ may be modified. Secondary interactions contribute less than 0.1% of the π^0 yield above p_T of 1 GeV/c and thus any distortions of $\langle \epsilon_\gamma f \rangle$ are negligible. Decays of K_s^0 are the predominate source of π^0 from weak decays. They contribute between 5.8% to 3% of the inclusive π^0 yield above 1 GeV/c. With $c\tau = 2.68$ cm, a fraction of 20% to 25% of those decays occur after the third but before the fourth layer of the VTX, which corresponds to the conversion photon sample used in this measurement. Therefore, in the data there are 1–2% more conversions in the fourth relative to the third layer compared to the MC simulation of primary π^0. The potential difference of $\langle \epsilon_\gamma f \rangle$ was estimated to be smaller than 1%.

C. Systematic uncertainty on $\gamma^{\rm hadr}/\gamma^{\pi^0}$

The ratio $\gamma^{\rm hadr}/\gamma^{\pi^0}$ accounts for photons from hadron decays that occur after the kinematic freeze, other than those from π^0. The three largest contributors are decays of η, ω, and η' mesons, which contribute ≈23% of the decay photons at high p_T. All other contributions to $\gamma^{\rm hadr}$ are negligible. Of the additional decay photons more than 80% are from the $\eta \to \gamma\gamma$ decay, hence the accuracy with which η/π^0 is known will determine the systematic uncertainties on R_γ from this source. The p_T and centrality dependent upper and lower bounds on η/π^0 for Au+Au collisions at $\sqrt{s_{NN}} = 200$ GeV are taken from [36]. Together with the much smaller uncertainty on the contribution from ω and η' decays, the systematic uncertainty on R_γ is below 2% for the entire p_T range.

D. Systematic uncertainties on $\gamma^{\rm dir}$

Once R_γ is determined, the direct-photon yield $\gamma^{\rm dir}$ is calculated as

$$\gamma^{\rm dir} = (R_\gamma - 1)\,\gamma^{\rm hadr}. \tag{9}$$

In addition to the uncertainties on R_γ, the uncertainty on $\gamma^{\rm hadr}$ needs to be determined. These systematic uncertainties have been studied in detail in [6]. The main sources of uncertainty come from the accuracy with which the π^0 p_T spectrum can be determined. These largely cancel in R_γ, but propagate directly to $\gamma^{\rm hadr}$. The input π^0 spectrum is based on measurements of charged pions and π^0 from different data-taking periods (see Sec. III D). Each data set comes with its own systematic uncertainties, and, in addition, the differences between different measurements are of the order of 10% [38]. The latter is the dominant uncertainty. The uncertainty on the spectra of other mesons (η, η', ω) also contributes to the uncertainty on $\gamma^{\rm hadr}$, but to a much smaller extent.

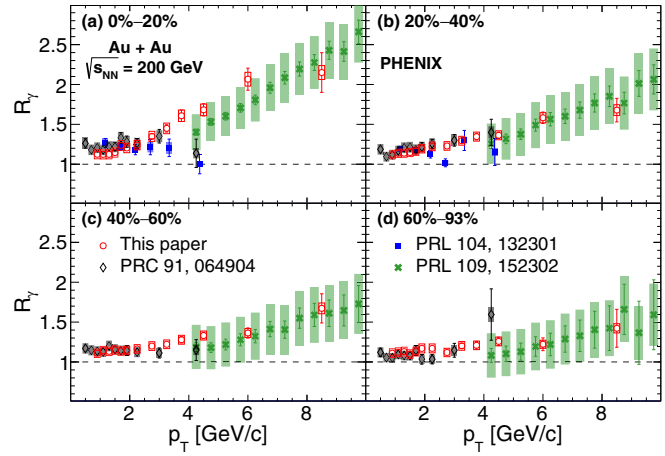

FIG. 12. The ratio $R_\gamma = \gamma^{\rm incl}/\gamma^{\rm hadr}$ as a function of conversion photon p_T in 0%–20%, 20%–40%, 40%–60% and 60%–93% centrality bins. The 2014 Au+Au data at $\sqrt{s_{NN}} = 200$ GeV are compared to results from previous PHENIX publications (see Refs. [3,6,39]).

V. RESULTS

A. Direct photon R_γ

Figure 12 shows R_γ as function of photon p_T for every 20% centrality class. The vertical error bar on each point corresponds to the statistical uncertainty, while the box gives the systematic uncertainty. The new results are compared with all other published PHENIX results for Au+Au at $\sqrt{s_{NN}} = 200$ GeV; these were obtained with different methods and have largely independent systematic uncertainties. The open circles were determined using the external conversion method deploying the HBD detector as converter [6], the full squares are from a virtual photon internal conversion measurement [4], and the open squares were measured with the EMCal alone [39]. All measurements agree well within their independent systematic uncertainties.

The 2014 data presented here have smaller statistical uncertainties than in previous publications at RHIC due to the increased luminosity and significantly larger amount of conversion material. The new results provide a continuous measurement across a wide range of p_T from 0.8 to 10 GeV/c. This range has previously been covered by measurements done with different techniques with different systematics. Up to 3 to 4 GeV/c internal or external photon conversions to e^+e^- pairs have been used, while above 4 GeV/c photons were measured in the EMCal. For all centrality selections, R_γ shows a significant excess that is rather constant below ≈3 GeV/c. Beyond that, R_γ increases with p_T, the increase being most pronounced for central collisions, and R_γ continuously decreases towards more peripheral collisions. This is expected as phenomena such as jet quenching reduce the number of decay photons from hadron decays in more central collisions, which in turn increases R_γ [33,35].

The high statistics of the 2014 data set allows one to divide the data sample into nine centrality bins, from 0%–10% to 80%–93%, 10% bins each, except for the last one which is

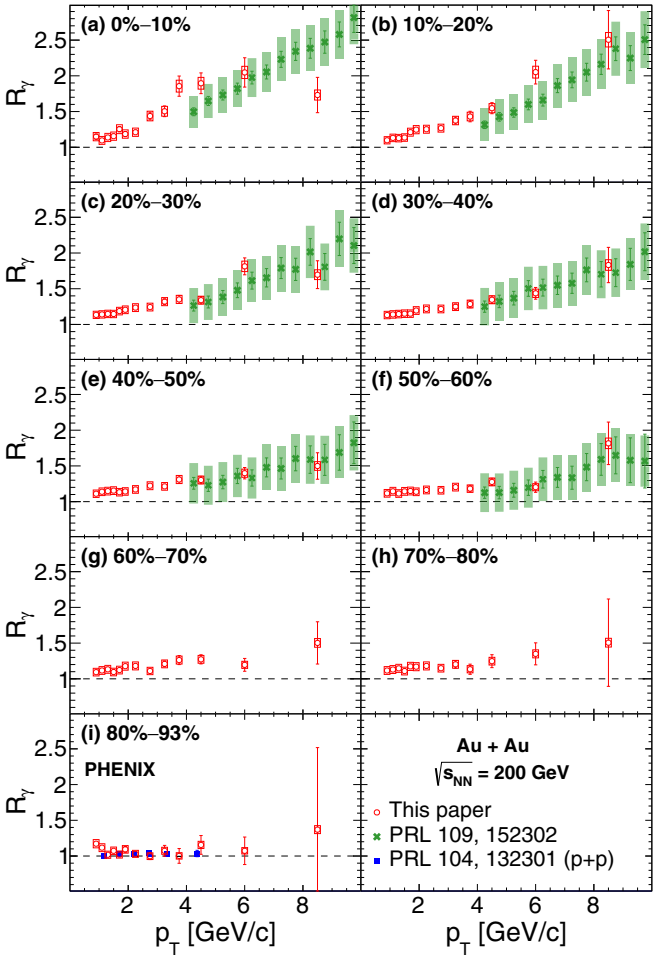

FIG. 13. R_γ of direct photons as a function of conversion photon p_T in 0%–10% to 80%–93% centrality bins. The 2014 Au+Au data at $\sqrt{s_{NN}} = 200$ GeV are compared to results from previous PHENIX publications (see Refs. [3,39]).

slightly larger. The resulting R_γ are shown in Fig. 13. Up to 50%–60% centrality, data from the earlier calorimeter measurement [39] are also shown.

For most bins the overall shape of R_γ as a function of p_T is similar to what is observed in Fig. 12, with a notable difference for panel (i), which is the most-peripheral centrality 80%–93%. Below 5 GeV/c, the most-peripheral Au+Au data show no significant excess above unity and are very consistent with the direct-photon result from $p+p$ collisions, which is also shown in panel (i).

The MC sampling method is used to calculate both the statistical and systematic uncertainties on $\gamma^{\rm dir}$ and all quantities derived from the direct photon p_T spectra. This method propagates the error correctly in the presence of unphysical values of $R_\gamma < 1$ and p_T and centrality dependent correlations of uncertainties; it is discussed in detail in Appendix B.

B. Direct-photon invariant yield

The direct-photon spectra are calculated from R_γ and $\gamma^{\rm hadr}$ using Eq. (9). The results for all 10% centrality selections

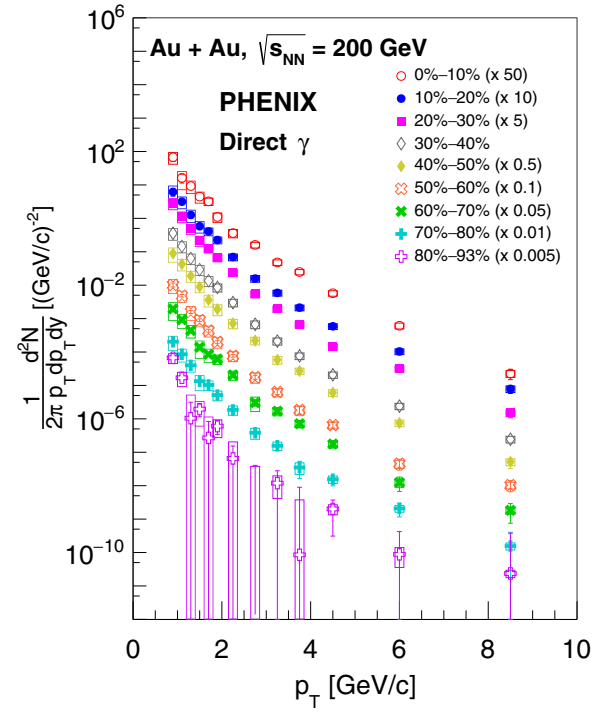

FIG. 14. Invariant yield of direct photons as a function of conversion photon p_T in 0%–10% to 80%–93% centrality bins.

are given in Fig. 14.[1] Figure 15 compares the direct-photon spectra with previous measurements, as shown in broader centrality bins (a) 0–20%, (b) 20–40%, (c) 40–60%, and (d) 60–93%. Each panel also presents the $N_{\rm coll}$-scaled perturbative quantum chromodynamics (pQCD) calculation [12] and a fit to direct-photon data from $p+p$ collisions at $\sqrt{s} = 200$ GeV [40–42]. The $p+p$ fit is performed with a pQCD-inspired functional form [43]:

$$\frac{d^3N}{d^2p_T dy} = \frac{A_{pp}}{\left(1+\left(\frac{p_T}{p_0}\right)^2\right)^n}, \tag{10}$$

where the parameters are $A_{pp} = 1.60\times10^{-4}$ (GeV/c)$^{-2}$, $p_0 = 1.45$ GeV/c and $n = 3.3$. The error band around the central fit function represents the uncertainty propagated from both the data and the unknown true functional form of the spectrum down to very low p_T. The $p+p$ fit and the pQCD calculation agree well above 2 GeV/c, and can be used as an estimate for the prompt-photon contribution.

Figure 15 also shows that the direct-photon yield for p_T larger than 5 GeV/c is well described by the $N_{\rm coll}$-scaled $p+p$ result and pQCD calculations, which confirms that the high-p_T direct photons are predominately from initial hard-scattering processes. Below 4–5 GeV/c a clear direct-photon excess develops above the prompt component, gradually becoming larger towards lower p_T.

[1]As the yields in the most-peripheral bin, 80%–93%, are mostly upper limits on the measurement, this bin will not be included for estimation of any further derived quantities in every 10% centrality selection.

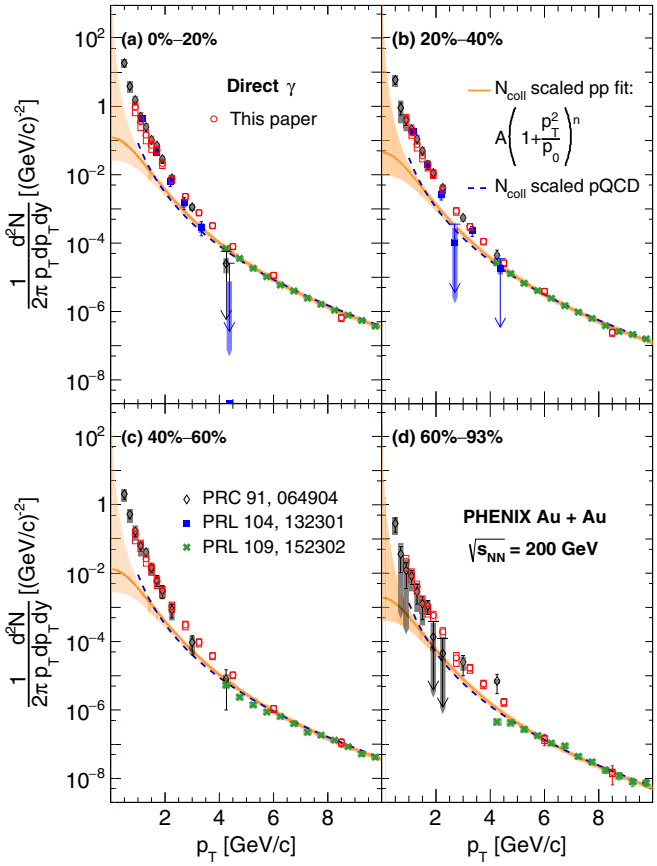

FIG. 15. Invariant yield of direct photons as a function of conversion photon p_T in (a) 0%–20%, (b) 20%–40%, (c) 40%–60%, and (d) 60%–93% centrality bins. The 2014 Au+Au data at $\sqrt{s_{NN}} = 200$ GeV are compared to results from previous PHENIX publications (see Refs. [3,6,39]).

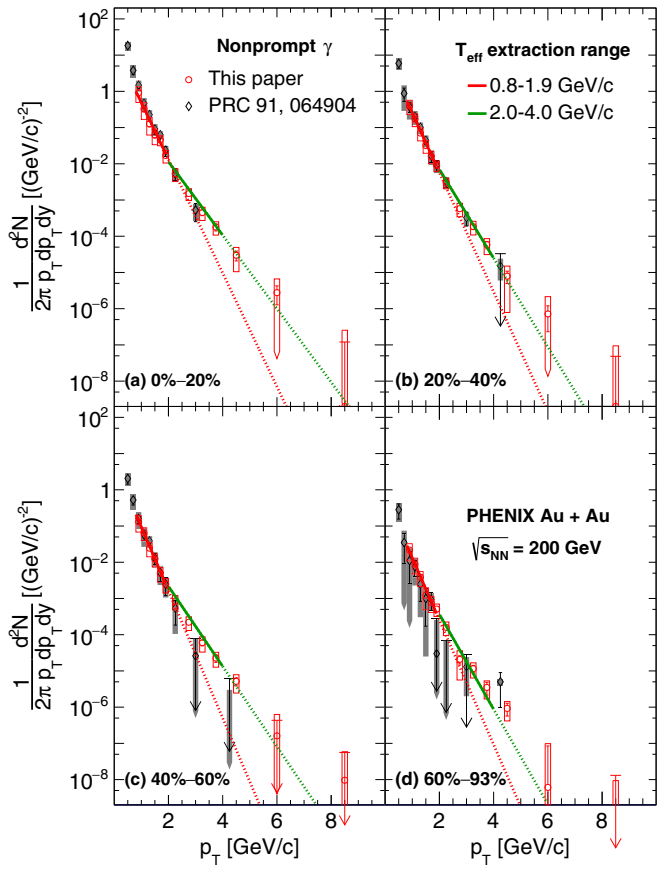

FIG. 16. Nonprompt direct-photon yield as a function of conversion photon p_T in (a) 0%–20%, (b) 20%–40%, (c) 40%–60%, and (d) 60%–93% centrality bins are compared to results from previous PHENIX publications (see Ref. [6]).

C. Nonprompt direct-photon excess

To extract the direct-photon excess above the prompt-photon contribution, the $N_{\rm coll}$ scaled $p+p$ fit is subtracted from the Au+Au data. This excess is thought to be mostly the radiation that is emitted during the collision from the hot-expanding fireball, and will be referred to here as nonprompt direct-photon spectra. Figure 16 compares the nonprompt direct-photon spectra to previously published results from Au+Au collisions at $\sqrt{s_{NN}} = 200$ GeV [6], which had significantly lower statistics. The new 2014 data extend the coverage, both in p_T and centrality.

The data are very consistent in the region of overlap. In the range 0.8 to 1.9 GeV/c, the data are fitted with an exponential function and the results are also shown on the panels of Fig. 16. The slope values are given in Table IV. All centrality selections are consistent with an average inverse slope, $T_{\rm eff}$, of $\approx 0.260 \pm 0.011$ GeV/c. However, it is evident from Fig. 16 that the nonprompt direct-photon spectra are not described by a single exponential but rather have an inverse slope $T_{\rm eff}$ that is continually increasing with p_T . Figure 17 brings this out more clearly where each nonprompt direct-photon spectrum is divided by a fit with a fixed slope, $T_{\rm eff} = 0.260$ GeV/c. All centrality selections follow the same trend. Over the p_T range of up to 2 GeV/c the ratios are consistent with unity, but above 2 GeV/c they start to rise monotonically.

To quantify this changing slope, the nonprompt direct-photon spectra are fitted with a second exponential function in the p_T range from 2 to 4 GeV/c; the results are also included in Fig. 16. All data are consistent with an average inverse slope of 0.376 ± 0.037 GeV/c, which is significantly larger than the slope observed below $p_T = 2$ GeV/c. Above 4 GeV/c, the statistical and systematic uncertainties from the prompt-photon subtraction become too large for a detailed analysis.

To establish any dependence on the system size, the nonprompt direct photon spectra are determined for each 10% centrality bin, and subsequently fitted by two exponential functions in the p_T ranges $0.8 < p_T < 1.9$ GeV/c and $2 < p_T < 4$ GeV/c. The resulting $T_{\rm eff}$ values are tabulated in Table IV and depicted in Fig. 18 as a function of $dN_{\rm ch}/d\eta$. The figure also shows the average of the inverse slope values from fitting Fig. 16. The $T_{\rm eff}$ values are consistent with a constant value, independent of $dN_{\rm ch}/d\eta$. However, given the uncertainties on the data, a possible increase of $T_{\rm eff}$ with $dN_{\rm ch}/d\eta$ can not be excluded.

In addition to investigating the p_T and system-size dependence of the shape of the nonprompt direct-photon spectra, one can also look at the dependence of the yield on system size

TABLE IV. Inverse slopes fitted to the direct-photon spectra in different p_T ranges, and for different centrality selections. For each centrality range, $N_{\rm coll}$ and $dN_{\rm ch}/d\eta$ values are quoted from previous work [44,45], except for the $dN_{\rm ch}/d\eta$ values for the two most peripheral bins. Those were extrapolated using a fit of the form $dN_{\rm ch}/d\eta = B(N_{\rm coll})^{\beta}$.

Centrality	$dN_{\rm ch}/d\eta$	$N_{\rm coll}$	$T_{\rm eff}$ (GeV/c) $0.8 < p_T < 1.9$ GeV/c	$T_{\rm eff}$ (GeV/c) $2 < p_T < 4$
0%–20%	519.2 ± 26.3	770.6 ± 79.9	$0.277 \pm 0.017\ ^{+0.036}_{-0.014}$	$0.428 \pm 0.031\ ^{+0.031}_{-0.030}$
20%–40%	225.4 ± 13.2	282.4 ± 28.4	$0.264 \pm 0.010\ ^{+0.014}_{-0.007}$	$0.354 \pm 0.019\ ^{+0.020}_{-0.030}$
40%–60%	85.5 ± 8.0	82.6 ± 9.3	$0.247 \pm 0.007\ ^{+0.005}_{-0.004}$	$0.392 \pm 0.023\ ^{+0.022}_{-0.022}$
60%–93%	16.4 ± 2.8	12.1 ± 3.1	$0.253 \pm 0.011\ ^{+0.012}_{-0.006}$	$0.331 \pm 0.036\ ^{+0.031}_{-0.041}$
0%–10%	623.9 ± 32.2	951 ± 98.5	$0.268 \pm 0.024\ ^{+0.026}_{-0.012}$	$0.514 \pm 0.061\ ^{+0.066}_{-0.039}$
10%–20%	414.2 ± 20.2	590.1 ± 61.1	$0.303 \pm 0.024\ ^{+0.062}_{-0.021}$	$0.358 \pm 0.033\ ^{+0.024}_{-0.035}$
20%–30%	274 ± 14.8	357.2 ± 35.5	$0.263 \pm 0.011\ ^{+0.014}_{-0.007}$	$0.351 \pm 0.024\ ^{+0.020}_{-0.030}$
30%–40%	176.8 ± 11.6	207.5 ± 21.2	$0.256 \pm 0.011\ ^{+0.009}_{-0.005}$	$0.333 \pm 0.024\ ^{+0.020}_{-0.032}$
40%–50%	109.4 ± 9.1	111.1 ± 10.8	$0.244 \pm 0.009\ ^{+0.003}_{-0.005}$	$0.389 \pm 0.029\ ^{+0.020}_{-0.021}$
50%–60%	61.6 ± 7.1	54.1 ± 7.9	$0.246 \pm 0.010\ ^{+0.005}_{-0.005}$	$0.345 \pm 0.031\ ^{+0.019}_{-0.032}$
60%–70%	32 ± 5	24 ± 6	$0.261 \pm 0.015\ ^{+0.020}_{-0.008}$	$0.319 \pm 0.049\ ^{+0.037}_{-0.042}$
70%–80%	16 ± 4	10 ± 3	$0.263 \pm 0.016\ ^{+0.016}_{-0.007}$	$0.335 \pm 0.044\ ^{+0.020}_{-0.035}$
80%–93%	7 ± 2	4 ± 1		

and p_T. As reported previously, the integrated direct-photon yield scales with $dN_{\rm ch}/d\eta$ to a power α [8]:

$$\frac{dN_\gamma}{dy} = \int_{p_{T,\rm min}}^{p_{T,\rm max}} \frac{dN_\gamma^{\rm dir}}{dp_T dy} dp_T = A \times \left(\frac{dN_{\rm ch}}{d\eta}\right)^{\alpha}, \qquad (11)$$

where all rapidity densities are densities at midrapidity. The direct-photon spectra shown in Fig. 14 are integrated from $p_{T,\rm min} = 1$ GeV/c to $p_{T\rm max} = 5$ GeV/c and plotted as a function of $dN_{\rm ch}/d\eta$ in Fig. 19. They are in reasonable agreement with a compilation of other direct-photon results [8,46], also shown in the figure. All data follow a trend similar to the $N_{\rm coll}$ scaled $p+p$ fit, shown as band, but at a roughly ten times larger yield. Scaling with $N_{\rm coll}$ corresponds to $\alpha = 1.25 \pm 0.02$ [8]. The current high statistics data allow for finer centrality binning and changes this picture somewhat at the lowest and highest $dN_{\rm ch}/d\eta$. Fitting only the new results in Fig. 19 gives a value of $\alpha = 1.11 \pm 0.02({\rm stat})\ ^{+0.09}_{-0.08}({\rm sys})$. This value is lower, but consistent within systematic uncertainties with $\alpha = 1.23 \pm 0.06 \pm 0.18$, found by fitting all previously published PHENIX $A+A$ data [46].

Note that the previous PHENIX measurements obtained the η spectrum by m_T scaling the π^0 spectrum, while in the current measurement the η spectrum is obtained from the η/π^0 ratio using the world data. There are significant differences between the two approaches in the low-p_T region [36]. Because the integration range starts at low p_T and is wide (1–5 GeV/c), the power α is smaller than previously

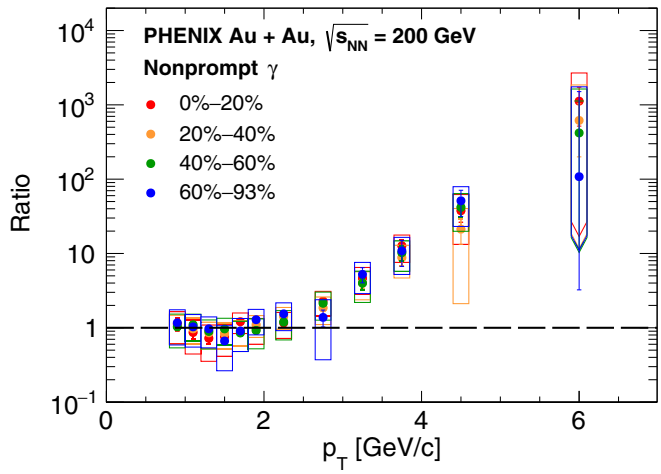

FIG. 17. Ratio of the yield of nonprompt direct photons over the exponential fit result ($T_{\rm eff}$ fixed to 0.26 GeV/c) as a function of photon p_T.

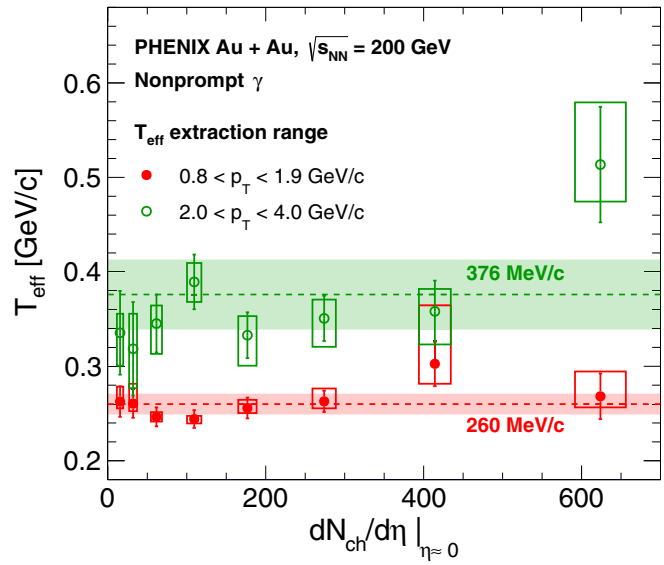

FIG. 18. $T_{\rm eff}$ as a function of charged-particle multiplicity at midrapidity.

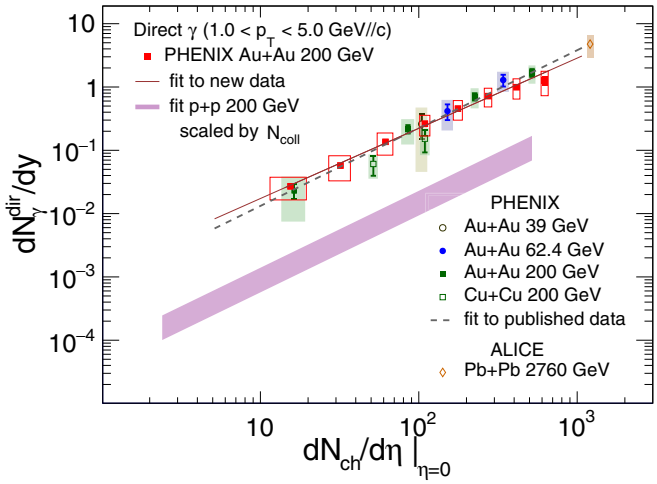

FIG. 19. Integrated direct-photon yield (1–5 GeV/c) versus charged-particle multiplicity at midrapidity. The present data are compared to a previous compilation of data from [8,46] and the $N_{\rm coll}$ scaled fit to $p+p$ data. Also given are fits with Eq. (11) to different data; the solid line is a fit to the present data resulting in $\alpha = 1.11 \pm 0.02({\rm stat})\,^{+0.09}_{-0.08}({\rm sys})$, and the dashed line is from fitting previously published PHENIX data [46] that gave $\alpha = 1.23 \pm 0.06 \pm 0.18$. The ALICE data are from Ref. [9].

published values, but is consistent within stated systematic uncertainties. However, it is also consistent with unity within uncertainties.

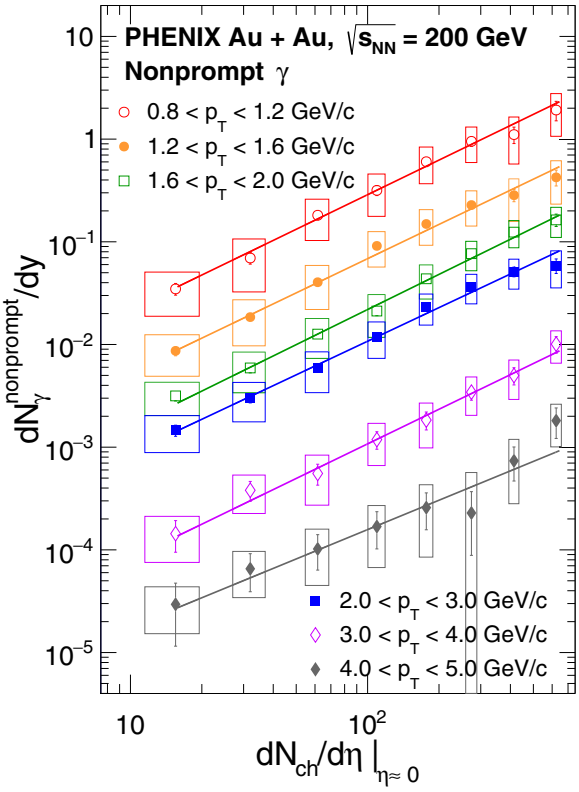

FIG. 20. Integrated nonprompt direct-photon yield versus charged particle multiplicity at midrapidity for different p_T integration ranges.

TABLE V. Scaling power, α, of the $dN_{\rm ch}/d\eta$ dependence of nonprompt and direct-photon yields in various integration ranges.

p_T (GeV/c)	$\alpha(\gamma^{\rm nonprompt})$	$\alpha(\gamma^{\rm dir})$
0.8–1.2	$1.119 \pm 0.038\,^{+0.116}_{-0.094}$	$1.124 \pm 0.036\,^{+0.121}_{-0.089}$
1.2–1.6	$1.107 \pm 0.029\,^{+0.108}_{-0.082}$	$1.118 \pm 0.027\,^{+0.097}_{-0.073}$
1.6–2.0	$1.136 \pm 0.034\,^{+0.129}_{-0.091}$	$1.152 \pm 0.029\,^{+0.113}_{-0.077}$
2.0–3.0	$1.087 \pm 0.032\,^{+0.108}_{-0.092}$	$1.120 \pm 0.025\,^{+0.095}_{-0.065}$
3.0–4.0	$1.119 \pm 0.078\,^{+0.206}_{-0.134}$	$1.171 \pm 0.048\,^{+0.114}_{-0.076}$
4.0–5.0	$0.950 \pm 0.176\,^{+0.315}_{-0.205}$	$1.137 \pm 0.077\,^{+0.108}_{-0.082}$
5.0–10.0		$1.296 \pm 0.078\,^{+0.129}_{-0.091}$

To better understand the behavior of the scaling power, α, in more detail, the direct-photon yield and its nonprompt component are integrated for six different nonoverlapping finer p_T regions and for 10% centrality classes. The integrated nonprompt yields are shown in Fig. 20. The α values are determined for each p_T selection by fitting the data with Eq. (11). The fits are also shown in the figure. All α values, for both the direct photon yield and the nonprompt component, are tabulated in Table V and shown in Fig. 21. It is evident that the values for the direct component, for higher p_T ranges, are consistent with the prompt component, $\alpha = 1.25 \pm 0.02$, corresponding to $N_{\rm coll}$ scaling. However, they tend to be smaller, but still consistent within systematic uncertainties, with previous measurements [8] for the lower p_T ranges.

With increasing p_T, the α values for the nonprompt component are slightly lower than those from direct photons. The systematic uncertainties are larger due to the subtraction. The values of α for the nonprompt component, as shown in Fig. 21, are remarkably constant with no evident p_T dependence.

VI. CONCLUDING DISCUSSION OF THE RESULTS

The PHENIX Collaboration has measured direct-photon production in Au+Au collisions at $\sqrt{s_{NN}} = 200$ GeV using

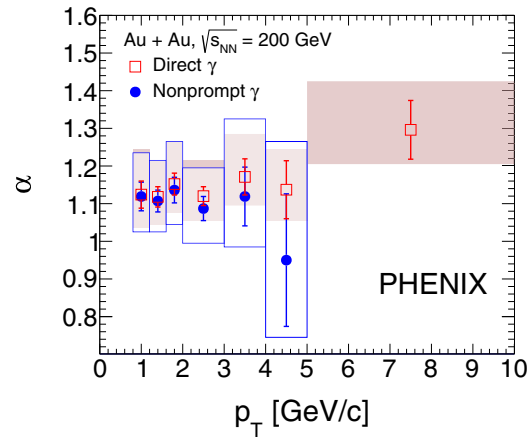

FIG. 21. Scaling factors, α, extracted from fitting Eq. (11) to integrated direct and nonprompt-photon yields as a function of $dN_{\rm ch}/d\eta$. Values were obtained for different p_T integration ranges tabulated in Table V.

photon conversions to e^+e^- pairs. A large yield of direct photons below a p_T of 3 GeV/c is observed for all centrality bins except for the most peripheral bin of 80%–93% with $dN_{\rm ch}/d\eta = 7.4$, where it seems to be consistent with the prompt-photon production. The next centrality bin from 70%–80% with $dN_{\rm ch}/d\eta = 15.5$ already shows a significant yield with properties very similar to that of the radiation from the more central bins.

The nonprompt direct-photon spectra are isolated by subtracting the prompt-photon contribution, which is estimated through a fit to the direct-photon data from $p+p$ collisions at $\sqrt{s} = 200$ GeV, measured by PHENIX, and scaled by $N_{\rm coll}$. Results are obtained for the p_T range from 0.8 to 5 GeV/c and for 0%–93% central collisions, covering a system size spanning two orders of magnitude in $dN_{\rm ch}/d\eta$ from ≈7 to 620. The wealth of data enabled PHENIX to carry out double-differential analyses of the shape of the momentum spectra and the rapidity density dN_γ/dy in p_T and $dN_{\rm ch}/d\eta$.

For the centrality selections from 0%–10% to 70%–80%, all nonprompt direct-photon spectra are very similar in shape, exhibiting increasing $T_{\rm eff}$ from 0.2 to 0.4 GeV/c over the p_T range from 0.8 to 4 GeV/c. The changing $T_{\rm eff}$ is not surprising, because the spectra are time integrated over the full evolution of the expanding fireball, from its earliest preequilibrium state, through the QGP phase, crossing over to a HG, and further expanding and cooling until hadrons eventually stop interacting. Throughout the evolution the system cools, and thus earlier phases are characterized by higher temperatures. In turn, the contributions from the earliest times of the evolution are likely to dominate the emission at higher p_T, consistent with the observation of an increasing $T_{\rm eff}$ with p_T.

In the lower p_T range from 0.8 to 1.9 GeV/c, the spectra are well described by a $T_{\rm eff} = 0.26$ GeV/c. This is consistent with what is expected for radiation from the late QGP stage until freeze-out [14]. During this period of the evolution, the temperature drops from ≈170 MeV near the transition to ≈110 MeV when the system freezes out. At the same time the system is rapidly expanding and thus, the radiation is blueshifted. This compensates the temperature drop and results in an average $T_{\rm eff} \approx 0.26$ GeV/c, with only minor variations with centrality of the collision. In Ref. [14], a moderate increase of $T_{\rm eff}$ with centrality was predicted. While the data favors a $T_{\rm eff}$ independent of centrality, they are not precise enough to exclude a moderate change.

Above a p_T of 2 GeV/c, the inverse slope of the spectra continues to increase with p_T. Between $p_T = 2$ and 4 GeV/c the average inverse slope is $T_{\rm eff}$ ≈0.376 GeV/c. This $T_{\rm eff}$ is larger than what model calculations for a rapidly expanding HG can accommodate, thus suggesting that emissions from the QGP phase and earlier times in the evolution starts to dominate the spectra. Expected initial temperatures at RHIC are ≈375 MeV with maximum $T_{\rm eff}$ in the range of 0.35 to 0.4 GeV/c, depending on viscosity [14]. Thus, it is likely that, in addition to photons from the QGP phase, photons from the pre-equilibrium stage are also needed to account for the measured $T_{\rm eff}$.

In Fig. 22, the measured nonprompt direct-photon spectra are compared to a recent calculation including contributions from the preequilibrium phase [10,47]. These calculations

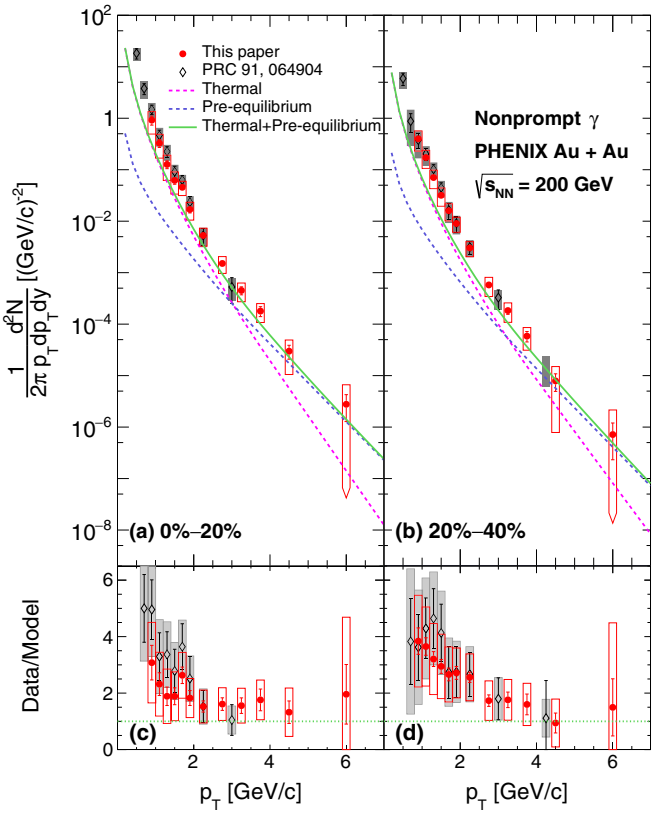

FIG. 22. Nonprompt direct-photon yields for (a) 0%–20% and (b) 20%–40% compared with model predictions from Refs. [10,47]. (c), (d) Ratios of the yields from data to the sum of yields from thermal and preequilibrium contributions. The 2014 Au+Au data at $\sqrt{s_{NN}} = 200$ GeV are compared to results from a previous PHENIX publications (see Ref. [6]).

predicted that the preequilibrium radiation becomes the dominant source above a p_T of 3 GeV/c. In the range $2 < p_T < 4$ GeV/c, a fit of the thermal contribution with an exponential function results in an inverse slope of ≈0.36 GeV/c, while for the preequilibrium contribution a larger inverse slope of ≈0.52 GeV/c is found, for the more central collisions. Fitting the same p_T range for the combined thermal and preequilibrium spectra from the model gives an inverse slope of ≈0.425 GeV/c. While the shape is reproduced well, the overall yield predicted by the calculations falls short compared to the data, in particular, below 2 GeV/c where the nonprompt-photon yield appears to be a factor of 2 to 3 larger.

The integrated nonprompt direct-photon yield exhibits a power-law relation with $(dN_{\rm ch}/d\eta)^\alpha$ [8]. Fitting the power α for multiple nonoverlapping p_T ranges results in values consistent with $\alpha = 1.12 \pm 0.06({\rm stat}) \pm 0.14({\rm sys})$ with no apparent dependence on p_T. The model calculations in [14] predict that the radiation from the HG phase scale with α close to 1.2, while those from the hot and dense QGP phase exhibit closer to a $(dN_{\rm ch}/d\eta)^2$ dependence. Because the QGP phase has a larger relative contribution to the p_T spectrum with increasing p_T, it is expected that α increases with p_T. However, the p_T dependence of α from the preequilibrium phase needs further theoretical understanding.

In conclusion, the tenfold increase in statistics compared to previous samples of Au+Au collisions recorded by PHENIX enabled detailed measurements of the radiation from the hot and expanding fireball. The experimentally observed inverse slopes of the p_T spectra are qualitatively consistent with predictions for thermal and preequilibrium radiation. However, there seem to be more photons emitted from Au+Au collisions than can be accounted for in model calculations. Furthermore, although this work presents no new data on the azimuthal anisotropy, maximum anisotropy is observed for photons ≈2–3 GeV/c. In this p_T range, the yield is larger than what would be expected from a rapidly but anisotropically expanding hadronic fireball. Finally, the centrality dependence of the nonprompt direct-photon yield, expressed in terms of the scaling power $\alpha(p_T)$, shows no indication of changing with p_T.

ACKNOWLEDGMENTS

We thank the staff of the Collider-Accelerator and Physics Departments at Brookhaven National Laboratory and the staff of the other PHENIX participating institutions for their vital contributions. We also thank J. F. Paquet for many fruitful discussions and sharing additional information. We acknowledge support from the Office of Nuclear Physics in the Office of Science of the Department of Energy, the National Science Foundation, Abilene Christian University Research Council, Research Foundation of SUNY, and Dean of the College of Arts and Sciences, Vanderbilt University (USA); Ministry of Education, Culture, Sports, Science, and Technology and the Japan Society for the Promotion of Science (Japan); Natural Science Foundation of China (People's Republic of China); Croatian Science Foundation and Ministry of Science and Education (Croatia); Ministry of Education, Youth and Sports (Czech Republic); Centre National de la Recherche Scientifique, Commissariat à l'Énergie Atomique, and Institut National de Physique Nucléaire et de Physique des Particules (France); J. Bolyai Research Scholarship, EFOP, the New National Excellence Program (ÚNKP), NKFIH, and OTKA (Hungary); Department of Atomic Energy and Department of Science and Technology (India); Israel Science Foundation (Israel); Basic Science Research and SRC(CENuM) Programs through NRF funded by the Ministry of Education and the Ministry of Science and ICT (Korea); Ministry of Education and Science, Russian Academy of Sciences, Federal Agency of Atomic Energy (Russia); VR and Wallenberg Foundation (Sweden); University of Zambia, the Government of the Republic of Zambia (Zambia); the U.S. Civilian Research and Development Foundation for the Independent States of the Former Soviet Union, the Hungarian American Enterprise Scholarship Fund, the US-Hungarian Fulbright Foundation, and the US-Israel Binational Science Foundation.

APPENDIX A: EVENT-MIXING PROCEDURES AND VALIDATION

In this analysis, e^+e^- pairs and $e^+e^-\gamma$ combinations result from combining positrons, electrons, and photons measured in the same event. Given the large multiplicity of produced particles in Au+Au collisions, the combinations include a significant background from particles of different physical origin, for example different π^0 decays. For e^+e^- pairs there are two possible combinations: signal pairs, $\mathrm{SG}^{\mathrm{ee}}$, that have the same source and background pairs, $\mathrm{BG}^{\mathrm{ee}}$, that have different sources. Both types will be combined with photons to get $e^+e^-\gamma$ combinations. There are three possibilities: A correlated e^+e^- pair is combined with a photon from the same source ($\mathrm{SG}^{ee\gamma}$); the e^+e^- pair is not correlated, but the photon is correlated to the e^+ or e^- ($\mathrm{BG}^{ee\gamma}_{\mathrm{corr}}$); or the photon is uncorrelated to the e^+e^- pair, irrespective whether it is $\mathrm{SG}^{\mathrm{ee}}$ or $\mathrm{BG}^{\mathrm{ee}}$ ($\mathrm{BG}^{ee\gamma}_{\mathrm{uncorr}}$).

All backgrounds are determined using event-mixing techniques that were developed and validated with MC studies of high-multiplicity events, for which a large sample of simulated π^0 events was generated. These events serve as pseudodata. The π^0 are generated according to the experimentally observed p_T spectrum, uniform in azimuthal angle, and with a constant rapidity density of $280\pi^0$, which corresponds to the typical π^0 multiplicity in the most central Au+Au collisions at $\sqrt{s_{NN}} = 200$ GeV.

From these pseudodata, N_γ^{incl} and $N_\gamma^{\pi^0,\mathrm{tag}}$ are extracted using the cuts and event-mixing schemes developed for the analysis of real data. They are corrected by $\langle\epsilon_\gamma f\rangle$, resulting in R_γ. Because in the pseudodata there are no other hadronic decay channels contributing to γ^{hadr} other than π^0, the R_γ from these pseudodata is given by

$$R_\gamma^{\mathrm{pseudo}} = \frac{N_\gamma^{\mathrm{incl}}}{N_\gamma^{\pi^0,\mathrm{tag}}} \times \langle\epsilon_\gamma f\rangle. \tag{A1}$$

As there are no direct photons in the pseudodata, the expected result would be $R_\gamma = 1$, within the statistical uncertainties of the simulation. The rest of this sections details each step of the R_γ determination from the pseudodata. The exact same procedure is also applied to the real data.

1. Determination of the inclusive photon yield N_γ^{incl}

Photon conversion candidates are created by combining e^+ and e^- from the same pseudodata event by requiring a valid conversion point within $1 < R < 29$ cm. This results in a foreground, $\mathrm{FG}^{\mathrm{ee}}$, containing a signal, $\mathrm{SG}^{\mathrm{ee}}$, that is, conversions of π^0 decay photons, and a background, $\mathrm{BG}^{\mathrm{ee}}$, where the e^+ and e^- come from conversion of two different π^0 decay photons. The background is determined by combining electrons and positrons from different pseudodata events, which are paired and subjected to the same cuts and conversion selection criteria. The mixed event background thus obtained, $\mathrm{MBG}^{\mathrm{ee}}$, is normalized to the foreground, $\mathrm{FG}^{\mathrm{ee}}$, in the mass region $0.16 < m_{e^+e^-} < 0.3$ GeV/c^2, which does not contain e^+e^- pairs from conversions (see Fig. 2 for reference).

Figure 23(a) shows the background, $\mathrm{MBG}^{\mathrm{ee}}$, obtained from the mixed event technique together with the true background, $\mathrm{BG}^{\mathrm{ee}}$, which was obtained from the MC ancestry information. Figure 23(b) shows the results (solid curve) after subtracting the mixed-event background from the foreground and (open symbols) subtracting the true background. Note that the two

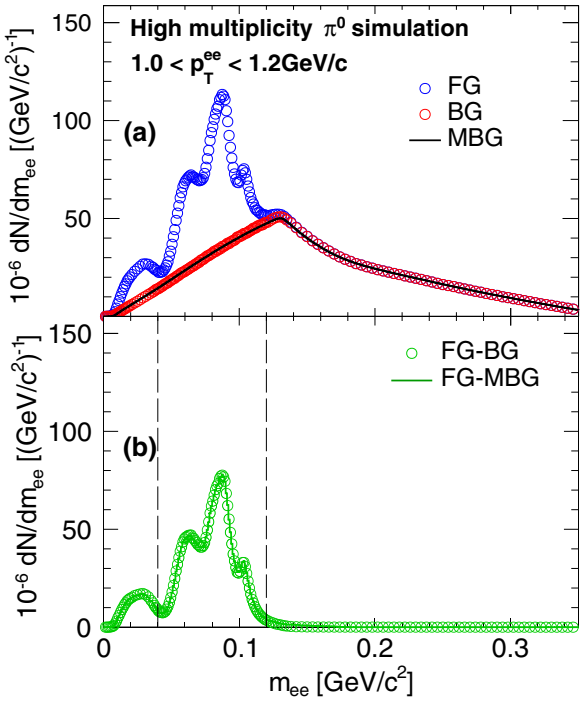

FIG. 23. Invariant mass distributions of e^+e^- pairs reconstructed from the high-multiplicity π^0 pseudodata in the p_T range $0.8 < p_T < 1.0$ GeV/c. The least-restrictive conversion selection cuts are applied, which only require that the reconstruction algorithm has identified the e^+e^- pair as a conversion candidate. Panel (a) compares foreground, FG^{ee}, the true background, BG^{ee}, and the background determined from the mixed event technique, MBG^{ee}. Panel (b) gives the extracted conversion photon signal.

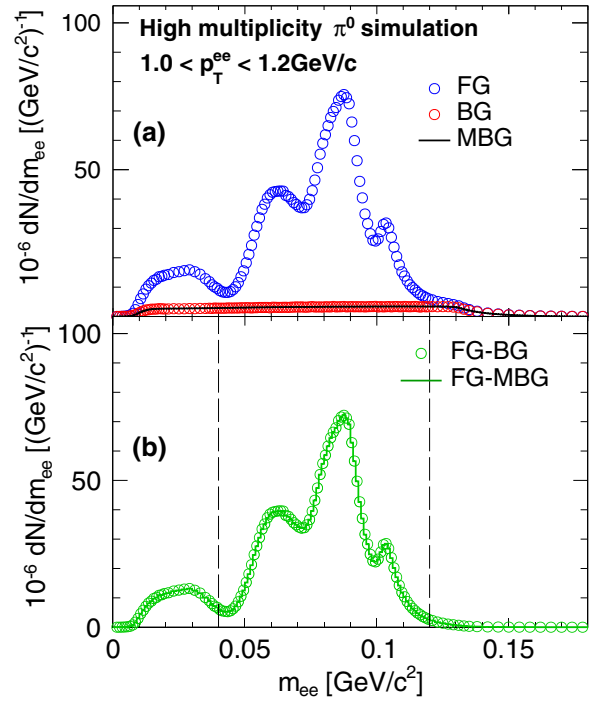

FIG. 24. Invariant mass distributions of e^+e^- pairs reconstructed from the high-multiplicity π^0 pseudodata. Same as Fig. 23, but with an additional constraint that the e^+ and e^- match in beam direction. Panel (a) compares foreground, FG^{ee}, the true background, BG^{ee}, and the background determined from the mixed event technique, MBG^{ee}. Panel (b) gives the extracted conversion photon signal.

are practically indistinguishable, which means that BG^{ee} is equal to MBG^{ee}.

Even though the background can be subtracted accurately with the mixed-event technique to obtain $N_\gamma^{\rm incl}$, the subtraction can only be done statistically. Thus in the next step, where conversion photons from π^0 decays are tagged, the background pairs also need to be matched with EMCal showers. This substantially increases the background in the $m_{ee\gamma}$ distribution. To reduce this background, additional cuts are applied in the conversion-photon selection.

The magnetic field deflects electrons and positrons in a plane perpendicular to the beam direction (z). Thus, e^+e^- pairs from a conversion can be constrained by requiring a match in the beam direction using the PC1 information. A cut of $|\Delta z| < 4$ cm is applied. Because the conversion reconstruction algorithm uses the projection of the tracks in the plane perpendicular to the beam axis, the additional match reduces the number of possible random-track combinations significantly. The z cut effectively truncates the mass distribution as the e^+e^- pairs are required to have the possible conversion point at radii below 29 cm and only the pairs with an opening angle in the beam direction will create larger masses. The background rejection is clearly visible in Fig. 24. The background normalization for the mixed events is given by the less restrictive cuts shown in Fig. 23, and applied here. For the lowest p_T and the highest-multiplicity bin, the background rejection is approximately a factor of 8 with a signal efficiency of more than 85%. The background to foreground ratio, BG^{ee}/FG^{ee}, is 12.1%. As p_T increases, the multiplicity decreases and the BG^{ee}/FG^{ee} ratio decreases to 0.3% at the p_T above 7 GeV/c.

The analysis is repeated for the entire accessible p_T range, and $N_\gamma^{\rm incl}$ is calculated in the mass range from 0.04 to 0.12 GeV/c^2 by subtracting the background obtained from the mixed-event technique, MBG^{ee}, from the foreground, FG^{ee}. The result is compared to the true number of photon conversions determined from the MC-ancestry information in Fig. 25. Panel (b) shows that the difference is less than 1% for all p_T.

2. The tagged photon yield $N_\gamma^{\pi^0,\rm tag}$

Next, the subset $N_\gamma^{\pi^0,\rm tag}$ of e^+e^- pairs in the $N_\gamma^{\rm incl}$ sample that can be tagged as photons from a π^0 decay is determined. For a given pseudodata event, each e^+e^- conversion candidate is paired with all reconstructed showers in the EMCal, excluding the showers matched to the e^+e^- pair itself. For each combination the invariant mass $m_{ee\gamma}$ is calculated. This constitutes the foreground, FG$^{ee\gamma}$, for which an example is given in panel (a) of Fig. 26. Despite the large background the signal $N_\gamma^{\pi^0,\rm tag}$ is clearly visible as peak around the π^0 mass. The background has two components: (i) combinations of e^+e^- pairs with an EMCal shower from another unrelated π^0

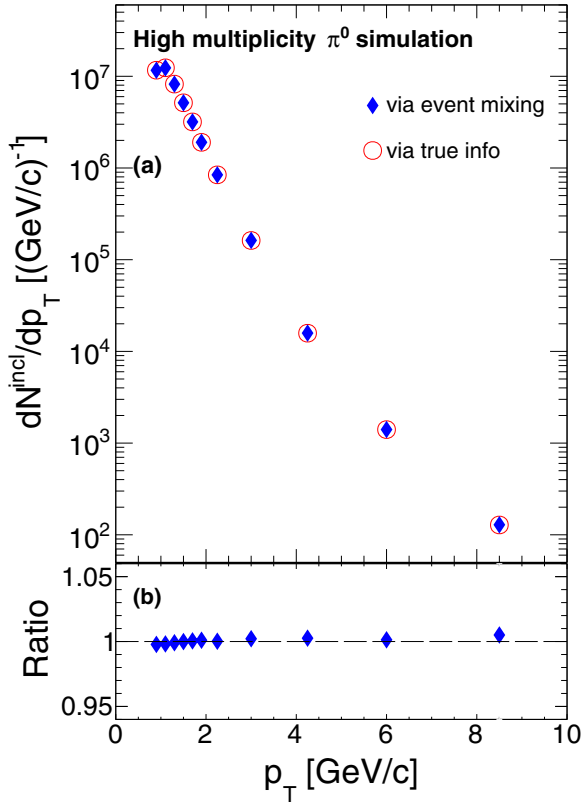

FIG. 25. Extracted $N_\gamma^{\rm incl}$ after the background subtraction, as a function of conversion photon p_T. The diamonds are obtained by subtracting the background from the mixed event technique; they are compared to the open symbols for which the true background was subtracted. Panel (b) shows the ratio of the event-mixing result over the true information result.

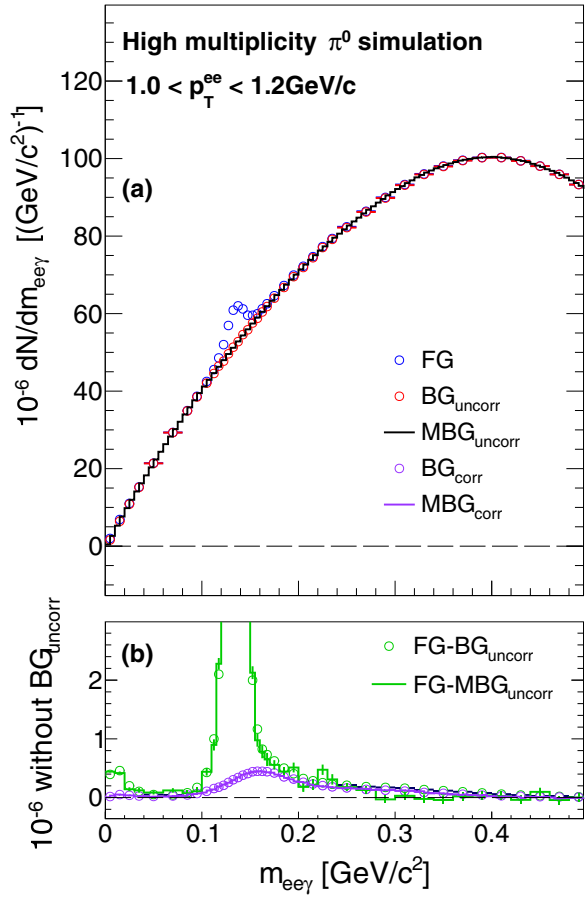

FIG. 26. Invariant mass distributions of $e^+e^-\gamma$ pairs.

decay denoted as $\mathrm{BG}^{ee\gamma}_{\rm uncorr}$, and (ii) a correlated background, $\mathrm{BG}^{ee\gamma}_{\rm corr}$, where the shower in the EMCal and the electron or positron are from the same π^0 decay, but the e^+e^- pair itself is a combination of an e^+ and e^- from different π^0 decay photons.

The uncorrelated background can be determined with an event mixing technique similar to that used for the extraction of $N_\gamma^{\rm incl}$: an e^+e^- pair from one event is mixed with the EMCal showers from a different event, resulting in mixed combinations $\mathrm{MBG}^{ee\gamma}_{\rm uncorr}$. These are normalized to the foreground, $\mathrm{FG}^{ee\gamma}$, in the mass region from 0.25 to 0.45 GeV/c^2, where no signal is expected. Figure 26(a) shows the corresponding distribution. There is almost no visible difference between the mixed-event background, $\mathrm{MBG}^{ee\gamma}_{\rm uncorr}$, and the true background, $\mathrm{BG}^{ee\gamma}_{\rm uncorr}$, which is obtained using the MC-ancestry information. Figure 26(b) shows the signal and remaining correlated background after the uncorrelated mixed-event background is subtracted ($\mathrm{FG}^{ee\gamma} - \mathrm{MBG}^{ee\gamma}_{\rm uncorr}$), as well as after subtracting the true uncorrelated background ($\mathrm{FG}^{ee\gamma} - \mathrm{BG}^{ee\gamma}_{\rm uncorr}$). Again they are indistinguishable.

The correlated background, $\mathrm{BG}^{ee\gamma}_{\rm corr}$, is determined with a second event-mixing scheme. An e^+ from a given event is combined with an e^- from a different event, and the resulting e^+e^- pair is then combined with the showers in the EMCal from both events; again excluding the showers from the e^+ and e^-. The $e^+e^-\gamma$ combinations contain the correlated background, $\mathrm{MBG}^{ee\gamma}_{\rm cor}$, plus the random background in which the e^+, e^-, and γ are from three different π^0 decays, $\mathrm{MBG}^{ee\gamma}_{\rm comb}$. The normalization is per generated e^+e^- pair, multiplied by $\mathrm{FG}^{ee\gamma}$, i.e., the number of background pairs in the e^+e^- pair foreground.

The random background, $\mathrm{MBG}^{ee\gamma}_{\rm comb}$, can easily be determined in a third event-mixing step, where e^+, e^-, and γ are from three different events. The $\mathrm{MBG}^{ee\gamma}_{\rm comb}$ is normalized to ($\mathrm{MBG}^{ee\gamma}_{\rm cor}$ +$\mathrm{MBG}^{ee\gamma}_{\rm comb}$) in the mass range from 0.65 to 1.0 GeV/c^2 and subtracted. Figure 27(a) shows the result, $\mathrm{MBG}^{ee\gamma}_{\rm cor}$, together with the foreground and the other background components.

Last but not least, to account for any possible mismatch between the true background and the one obtained from our multistep event-mixing procedure, the ratio ($\mathrm{FG}^{ee\gamma} - \mathrm{MBG}^{ee\gamma}_{\rm cor} - \mathrm{MBG}^{ee\gamma}_{\rm uncorr}$)/$\mathrm{MBG}^{ee\gamma}_{\rm uncorr}$ is fit with a second-order polynomial, $f_{ee\gamma}$, excluding the π^0 peak regions. The fit result is shown as a line on Fig. 27(b). This fit is used to correct $\mathrm{MBG}^{ee\gamma}_{\rm uncorr}$ before subtraction. The final distribution for $N_\gamma^{\pi^0,\rm tag}$ is thus

$$N_\gamma^{\pi^0,\rm tag} = \mathrm{FG}^{ee\gamma} - \mathrm{MBG}^{ee\gamma}_{\rm cor} - (1 + f_{ee\gamma})\,\mathrm{MBG}^{ee\gamma}_{\rm uncorr}. \quad \text{(A2)}$$

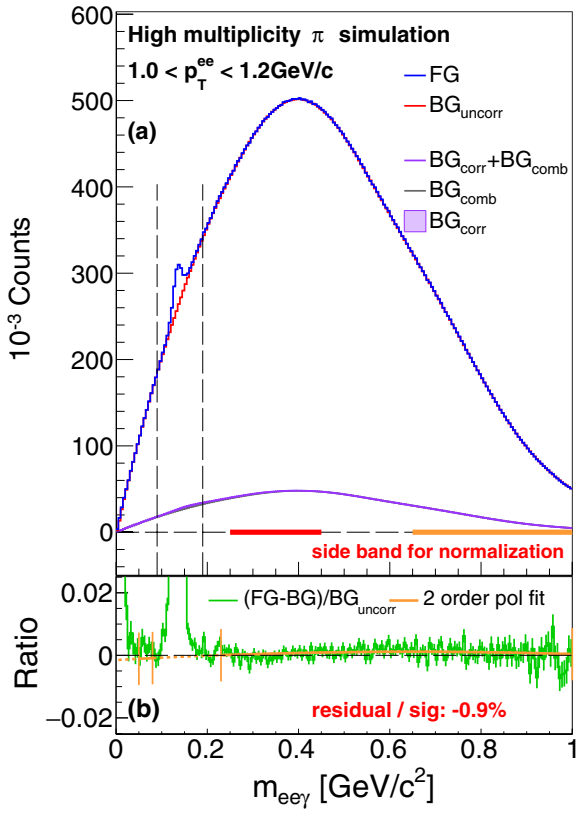

FIG. 27. Invariant mass distributions of $e^+e^-\gamma$ pairs from the same event (FG) and different event-mixing setups.

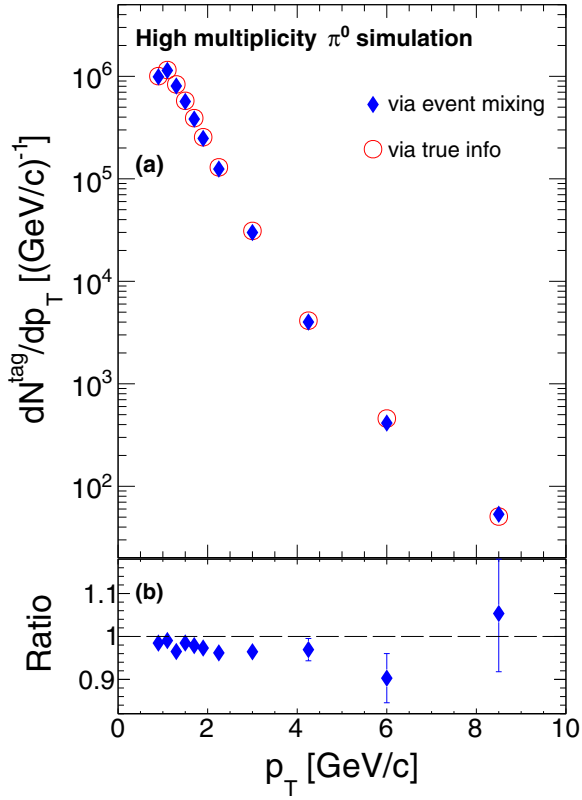

FIG. 28. Extracted $N_\gamma^{\pi^0,\mathrm{tag}}$ as a function of conversion-photon p_T using the (red) true information and (blue) event-mixing technique. The bottom panel shows the ratio of the event-mixing result over the true information result.

For each p_T bin, $N_\gamma^{\pi^0,\mathrm{tag}}$ is extracted by counting the number of entries in a window around the π^0 peak, $(0.09 < m_{ee\gamma} < 0.19)$ GeV/c^2. Figure 28 shows $N_\gamma^{\pi^0,\mathrm{tag}}$ as function of p_T using the true MC-ancestry information and the event-mixing technique. Overall the agreement is very good; however, the result from the event-mixing technique is on average lower. This mismatch is accounted for in the systematic uncertainties on R_γ, which is discussed in more detail in the next section.

3. Completing the validation by determining R_γ

With N_γ^{incl} and $N_\gamma^{\pi^0,\mathrm{tag}}$ established from the pseudodata, the conditional probability $\langle \epsilon_\gamma f \rangle$ remains to be determined to calculate R_γ and to fully validate the background-subtraction procedure. In the same way as for the data, a single π^0 simulation is embedded into pseudodata events. The e^+e^- pairs and $e^+e^-\gamma$ combinations are reconstructed and counted as discussed in Sec. III C. The extracted $\langle \epsilon_\gamma f \rangle$ is shown in Fig. 29 as a function of the conversion photon p_T.

With $N_\gamma^{\mathrm{incl}}/N_\gamma^{\pi^0,\mathrm{tag}}$ from the pseudodata and $\langle \epsilon_\gamma f \rangle$ from the embedded single π^0 simulation in hand, R_γ is calculated using Eq. (A1). The result is shown in Fig. 30; all points are close to unity, indicating that the analysis procedure is self-consistent. There may be a 1.5% enhancement above unity, which is consistent with the slightly lower-than-expected value found for $N_\gamma^{\pi^0,\mathrm{tag}}$. This difference is taken into account in the estimate of the systematic uncertainty.

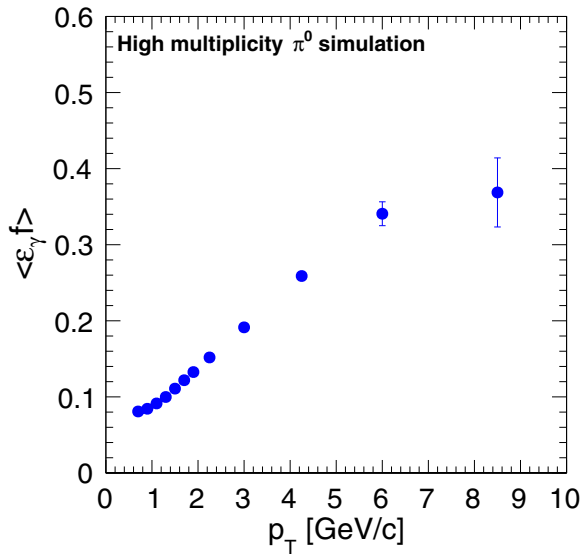

FIG. 29. Average conditional probability $\langle \epsilon_\gamma f \rangle$ as a function of conversion photon p_T.

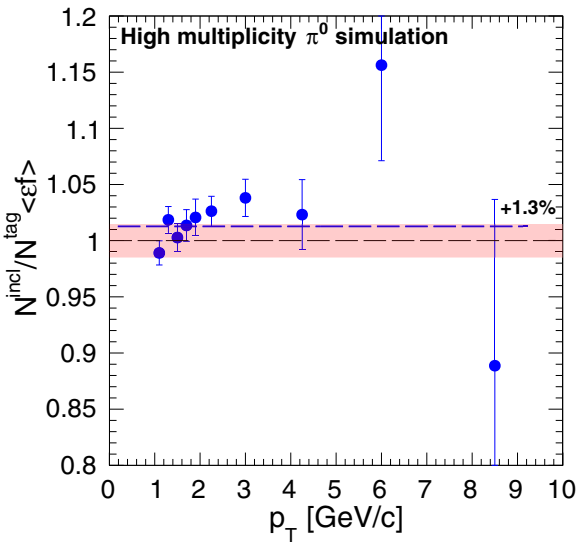

FIG. 30. Ratio R_γ^{pseudo} as a function of conversion photon p_T. The dashed line gives a constant offset of 1.3% fit to the points, and the dashed band represents a ±1.5% range around unity.

APPENDIX B: UNCERTAINTY PROPAGATION WITH A MC-SAMPLING METHOD

The uncertainties on γ^{dir} and any other quantity derived from γ^{dir}, such as T_{eff} or α, are determined using a MC-sampling method, which allows taking into account the p_T and centrality dependent correlations of individual sources of systematic uncertainties, as well as the fact that the region $R_\gamma < 1$ is unphysical.

1. Systematic uncertainties

In the MC-sampling method, for each source of uncertainty, i, a variation δ_i of R_γ or γ^{hadr} is sampled from a Gaussian distribution centered at zero with a width corresponding to the associated uncertainty, σ_i. The size of δ_i depends not only on σ_i, but also on whether the adjacent bins in p_T and centrality have uncorrelated (Type A) or correlated (Type B/C) uncertainties due to the source i. The values of σ_i and classification of each source is summarized in Table III.

If source i is classified as uncorrelated, δ_i is calculated independently for neighboring bins from Gaussian distributions of width σ_i. For correlated uncertainties of Type C in p_T or centrality, δ_i is calculated with one common fraction w so that $\delta_i = w\sigma_i$ for all points. The fraction w is determined randomly from a Gaussian distribution of width 1. And finally, for Type B uncertainties, δ_i is determined separately for the minimum and maximum of the p_T or centrality range using the same procedure as Type C. All intermediate points are varied proportionally to create a smooth transition from the minimum to the maximum of the range. Uncertainties on the input π^0 p_T distribution are a special case of Type B uncertainties, as it is known that the systematic uncertainties move simultaneously either up or down. In this case, δ_i at the minimum and maximum of the range are chosen to have the same sign.

After applying all variations δ_i to recalculate R_γ and γ^{hadr}, new values of γ^{dir}, T_{eff}, and α are determined. This process is repeated multiple times, taking into account the different sources of uncertainties, to obtain a distributions of γ^{dir}, T_{eff}, and α. The width of each distribution is quoted as their systematic uncertainty. For individual γ^{dir} points, it is possible that $\langle\gamma^{\text{dir}}\rangle - \sigma$ is less than 0, that is, unphysical. In such cases, an upper limit of 90% confidence level (CL) is quoted based on the part of the probability distribution in the physical region $\int_0^{\text{upper}} / \int_0^{+\infty} = 90\%$.

2. Statistical uncertainties

The statistical uncertainties on R_γ are assumed to have a Gaussian probability distribution, and for most cases the statistical uncertainty on γ^{dir} can be calculated with the usual error propagation. However, there are two cases that need to be treated separately:

(i) $R_\gamma < 1$: In this case γ^{dir} is unphysical, and hence an upper limit at 90% CL is quoted, based on the physical part of the probability distribution $\int_0^{\text{upper}} / \int_0^{+\infty} = 90\%$.

(ii) $R_\gamma - \sigma_{\text{stat}} < 1$: In this case γ^{dir} is in the physical region, but is consistent with zero within less than one standard deviation. For these situations the central value is shown, but the uncertainty is given as 90% CL, calculated as above.

[1] E. V. Shuryak, Quark-gluon plasma and hadronic production of leptons, photons and psions, Phys. Lett. B **78**, 150 (1978).

[2] G. David, Direct real photons in relativistic heavy ion collisions, Rep. Prog. Phys. **83**, 046301 (2020).

[3] A. Adare *et al.* (PHENIX Collaboration), Enhanced production of direct photons in Au+Au collisions at $\sqrt{s_{NN}} = 200$ GeV and implications for the initial temperature, Phys. Rev. Lett. **104**, 132301 (2010).

[4] A. Adare *et al.* (PHENIX Collaboration), Observation of direct-photon collective flow in $\sqrt{s_{NN}} = 200$ GeV Au+Au collisions, Phys. Rev. Lett. **109**, 122302 (2012).

[5] A. Adare *et al.* (PHENIX Collaboration), Azimuthally anisotropic emission of low-momentum direct photons in Au+Au collisions at $\sqrt{s_{NN}} = 200$ GeV, Phys. Rev. C **94**, 064901 (2016).

[6] A. Adare *et al.* (PHENIX Collaboration), Centrality dependence of low-momentum direct-photon production in Au+Au collisions at $\sqrt{s_{NN}} = 200$ GeV, Phys. Rev. C **91**, 064904 (2015).

[7] L. Adamczyk *et al.* (STAR Collaboration), Direct virtual photon production in Au + Au collisions at $\sqrt{s_{NN}} = 200$ GeV, Phys. Lett. B **770**, 451 (2017).

[8] A. Adare *et al.* (PHENIX Collaboration), Beam energy and centrality dependence of direct-photon emission from

ultrarelativistic heavy-ion collisions, Phys. Rev. Lett. **123**, 022301 (2019).
[9] J. Adam *et al.* (ALICE Collaboration), Direct photon production in Pb-Pb collisions at $\sqrt{s_{NN}} = 2.76$ TeV, Phys. Lett. B **754**, 235 (2016).
[10] C. Gale, J.-F. Paquet, B. Schenke, and C. Shen, Multimessenger heavy-ion collision physics, Phys. Rev. C **105**, 014909 (2022).
[11] O. Linnyk, E. L. Bratkovskaya, and W. Cassing, Effective QCD and transport description of dilepton and photon production in heavy-ion collisions and elementary processes, Prog. Part. Nucl. Phys. **87**, 50 (2016).
[12] J.-F. Paquet, C. Shen, G. S. Denicol, M. Luzum, B. Schenke, S. Jeon, and C. Gale, Production of photons in relativistic heavy-ion collisions, Phys. Rev. C **93**, 044906 (2016).
[13] L. McLerran and B. Schenke, The glasma, photons and the implications of anisotropy, Nucl. Phys. A **929**, 71 (2014).
[14] C. Shen, U. W. Heinz, J.-F. Paquet, and C. Gale, Thermal photons as a quark-gluon plasma thermometer reexamined, Phys. Rev. C **89**, 044910 (2014).
[15] H. van Hees, C. Gale, and R. Rapp, Thermal photons and collective flow at the Relativistic Heavy-Ion Collider, Phys. Rev. C **84**, 054906 (2011).
[16] K. Dusling and I. Zahed, Thermal photons from heavy ion collisions: A spectral function approach, Phys. Rev. C **82**, 054909 (2010).
[17] M. Dion, J.-F. Paquet, B. Schenke, C. Young, S. Jeon, and C. Gale, Viscous photons in relativistic heavy ion collisions, Phys. Rev. C **84**, 064901 (2011).
[18] H. van Hees, M. He, and R. Rapp, Pseudo-critical enhancement of thermal photons in relativistic heavy-ion collisions? Nucl. Phys. A **933**, 256 (2015).
[19] J. Berges, K. Reygers, N. Tanji, and R. Venugopalan, Parametric estimate of the relative photon yields from the glasma and the quark-gluon plasma in heavy-ion collisions, Phys. Rev. C **95**, 054904 (2017).
[20] M. Heffernan, P. Hohler, and R. Rapp, Universal parametrization of thermal photon rates in hadronic matter, Phys. Rev. C **91**, 027902 (2015).
[21] O. Linnyk, V. Konchakovski, T. Steinert, W. Cassing, and E. L. Bratkovskaya, Hadronic and partonic sources of direct photons in relativistic heavy-ion collisions, Phys. Rev. C **92**, 054914 (2015).
[22] G. Başar, D. E. Kharzeev, and V. Skokov, Conformal anomaly as a source of soft photons in heavy ion collisions, Phys. Rev. Lett. **109**, 202303 (2012).
[23] G. Başar, D. E. Kharzeev, and E. V. Shuryak, Magneto-sonoluminescence and its signatures in photon and dilepton production in relativistic heavy ion collisions, Phys. Rev. C **90**, 014905 (2014).
[24] B. Müller, S.-Y. Wu, and D.-L. Yang, Elliptic flow from thermal photons with magnetic field in holography, Phys. Rev. D **89**, 026013 (2014).
[25] M. Allen *et al.* (PHENIX Collaboration), PHENIX inner detectors, Nucl. Instrum. Methods Phys. Res. Sect. A **499**, 549 (2003).
[26] K. Adcox *et al.* (PHENIX Collaboration), PHENIX detector overview, Nucl. Instrum. Methods Phys. Res. Sect. A **499**, 469 (2003).
[27] A. Taketani (PHENIX Collaboration), A silicon vertex tracker for PHENIX, Nucl. Phys. A **774**, 911 (2006).
[28] K. Adcox *et al.* (PHENIX Collaboration), PHENIX central arm tracking detectors, Nucl. Instrum. Methods Phys. Res. Sect. A **499**, 489 (2003).
[29] J. T. Mitchell *et al.* (PHENIX Collaboration), Event reconstruction in the PHENIX central arm spectrometers, Nucl. Instrum. Methods Phys. Res. Sect. A **482**, 491 (2002).
[30] M. Aizawa *et al.* (PHENIX Collaboration), PHENIX central arm particle ID detectors, Nucl. Instrum. Methods Phys. Res. Sect. A **499**, 508 (2003).
[31] L. Aphecetche *et al.* (PHENIX Collaboration), PHENIX calorimeter, Nucl. Instrum. Methods Phys. Res., Sect. A **499**, 521 (2003).
[32] R. Brun, F. Bruyant, M. Maire, A. C. McPherson, and P. Zanarini, GEANT3, 1987.
[33] S. S. Adler *et al.* (PHENIX Collaboration), Suppressed π^0 production at large transverse momentum in central Au + Au collisions at $\sqrt{s_{NN}} = 200$ GeV, Phys. Rev. Lett. **91**, 072301 (2003).
[34] S. S. Adler *et al.* (PHENIX Collaboration), Identified charged particle spectra and yields in Au+Au collisions at $\sqrt{s_{NN}} = 200$ GeV, Phys. Rev. C **69**, 034909 (2004).
[35] A. Adare *et al.* (PHENIX Collaboration), Suppression pattern of neutral pions at high transverse momentum in Au+Au collisions at $\sqrt{s_{NN}} = 200$ GeV and constraints on medium transport coefficients, Phys. Rev. Lett. **101**, 232301 (2008).
[36] Y. Ren and A. Drees, Examination of the universal behavior of the η-to-$\pi 0$ ratio in heavy-ion collisions, Phys. Rev. C **104**, 054902 (2021).
[37] A. Adare *et al.* (PHENIX Collaboration), Spectra and ratios of identified particles in Au + Au and d + Au collisions at $\sqrt{s_{NN}} = 200$ GeV, Phys. Rev. C **88**, 024906 (2013).
[38] A. Adare *et al.* (PHENIX Collaboration), Heavy quark production in $p + p$ and energy loss and flow of heavy quarks in Au+Au collisions at $\sqrt{s_{NN}} = 200$ GeV, Phys. Rev. C **84**, 044905 (2011).
[39] S. Afanasiev *et al.* (PHENIX Collaboration), Measurement of direct photons in Au + Au collisions at $\sqrt{s_{NN}} = 200$ GeV, Phys. Rev. Lett. **109**, 152302 (2012).
[40] S. S. Adler *et al.* (PHENIX Collaboration), Measurement of direct photon production in $p + p$ collisions at $\sqrt{s} = 200$ GeV, Phys. Rev. Lett. **98**, 012002 (2007).
[41] A. Adare *et al.* (PHENIX Collaboration), Direct-photon production in $p + p$ collisions at $\sqrt{s} = 200$ GeV at midrapidity, Phys. Rev. D **86**, 072008 (2012).
[42] A. Adare *et al.* (PHENIX Collaboration), Direct photon production in d+Au collisions at $\sqrt{s_{NN}} = 200$ GeV, Phys. Rev. C **87**, 054907 (2013).
[43] A. Adare *et al.* (PHENIX Collaboration), Low-momentum direct-photon measurement in Cu+Cu collisions at $\sqrt{s_{NN}} =$ 200 GeV, Phys. Rev. C **98**, 054902 (2018).
[44] S. S. Adler *et al.* (PHENIX Collaboration), Systematic studies of the centrality and $\sqrt{s_{NN}}$ dependence of the $dE_T/d\eta$ and $dN_{\rm ch}/d\eta$ in heavy ion collisions at rapidity, Phys. Rev. C **71**, 034908 (2005); Publisher's Note: Systematic studies of the centrality and $\sqrt{s_{NN}}$ dependence of the $dE_T/d\eta$ and $dN_{\rm ch}/d\eta$ in heavy ion collisions at rapidity [Phys. Rev. C 71, 034908 (2005)], **71**, 049901(E) (2005).

[45] A. Adare *et al.* (PHENIX Collaboration), Transverse energy production and charged-particle multiplicity at midrapidity in various systems from $\sqrt{s_{NN}} = 7.7$ to 200 GeV, Phys. Rev. C **93**, 024901 (2016).

[46] N. J. Abdulameer *et al.* (PHENIX Collaboration), Low-pT direct-photon production in Au+Au collisions at $\sqrt{s_{NN}} = 39$ and 62.4 GeV, Phys. Rev. C **107**, 024914 (2023).

[47] J. F. Paquet (private communication).